January 2020

Parylene Based Flexible Multifunctional Biomedical Probes And Their Applications

Zhiguo Zhao
Wayne State University

PARYLENE BASED FLEXIBLE MULTIFUNCTIONAL BIOMEDICAL PROBES AND THEIR APPLICATIONS

by

ZHIGUO ZHAO

DISSERTATION

Submitted to the Graduate School

of Wayne State University,

Detroit, Michigan

in partial fulfillment of the requirements

for the degree of

DOCTOR OF PHILOSOPHY

2020

MAJOR: ELECTRICAL AND COMPUTER ENGINEERING

Approved By:

Advisor Date

DEDICATION

I dedicate this work to those without whom I couldn't have finished this long journey.

To my parents, Shengji Zhao and Qingzi Che who always support and believe in me for whatever I do.

To my family, Jinhee Lee, and my daughter Ellie Zhao who is the only reason that I make it here.

To my advisor Yong Xu; my committee members Mark Cheng, Jinsheng Zhang, and Dimitrios Sounas; my lab mates Eric Kim, Xiaoyu Chen and Xiaoce Feng. I couldn't finish this journey without your endless support and help.

ACKNOWLEDGMENTS

A lot of support with fabrication and characterization was provided by Xiaoyu Chen, Xiaoce Feng, and Eric Kim. Some characterization equipment, as well as assistance, was provided by Mark Cheng and his group including Boshen Zhang, Gui Chen. Assistance with SEM was provided by Dr. Mei Zhi.

Some material in this work was reprinted with permission from other sources. Where appropriate, this is indicated by a footnote crediting the original source.

TABLE OF CONTENTS

List of Figures

Chapter 1 : Introduction

Background

MEMS-based flexible devices have been extensively studied for decades. From various wearable electronics to miniaturized tools for cutting-edge researches, these flexible devices have become indispensable components of our daily lives and solved many scientific challenges. Flexible textures and skins, a typical example of flexible electronics, have been constructed in different forms for a diversity of applications [1]. Rakesh et al. integrated silicon flexible skins with canvas fabrics by a sewing machine [2]. The reported technology allowed various sensing capabilities to be incorporated into flexible fabrics without losing its durability and mechanical strength. Huang et al. reported a yarn-based piezo-resistive sensor by twisting piezo-resistive polyester fibers, and successfully demonstrated its feasibility of being used in the respiration monitoring system [3]. Based on the technology of 2-dimensional flexible texture and skin, advanced flexible yarns and tubes have also been studied and developed for some pivotal applications [4]. Wu et al. reported a flexible and conductive nanofiber-based yarn sensor for ammonia (NH_3) detecting [5]. The conductive yarn was made by combining core-sheath polyaniline (PANI) and polyacrylonitrile (PAN) through the electrospinning method. Tao et al. and Yalong et al. developed a flexible strain sensor with excellent mechanical and electrical properties by using carbon/graphene composites thermoplastic polyurethane yarn, which also can be readily incorporated with textiles for various applications [6, 7].

The flexible MEMS technology has contributed significantly to biomedical researches such as neural activity exploration and cell culture. For example, recently

flexible neural probes have been replacing traditional rigid silicon-based probes mainly due to their less adverse effect on brains and tissues [8-12]. Benefits of flexible biocompatible probes have been demonstrated, and many efforts have been spent not only on improving the durability, stability, and feasibility, but also providing superb performance and multiple functionalities [13-16]. In the next section, a series of different types of biomedical probes will be reviewed, and the pros and cons of each type will be discussed.

Literature review

With the rapid advance of microfabrication technology, a large variety of biomedical sensors and devices in the form factor of micro probes or needles have been developed [17, 18]. The microfabrication technology enables the integration of various sensing elements such as pH or oxygen sensors [19], and the adoption of multiple electrode arrays (MEAs) for better spatial resolution [20-22]. In addition, recent studies have been focusing on integrating multiple functionalities into microfabricated probes such as drug delivery and optogenetics to realize simultaneous measurements of multiple chemicals and multiplexed interactions between electrodes and tissues [23, 24]. Hence, this section will outline the early and recent research on the microfabricated probes and their applications.

The most common type of biomedical probes is neural probe which is widely used for neural recording and stimulating such as deep brain stimulation (DBS). Neural probes are designed for invasive analysis due to their better resolution and accuracy compared to electroencephalography (EEG) and electrocorticography (ECoG) technologies. Early studies exploited microwire arrays (MWAs) due to the relatively simple assembly and

long-term stability for chronical brain signal monitoring [25]. Various commercially accessible metals or metal alloys are employed including tungsten, platinum, gold, and platinum-iridium alloys [26-29]. Nevertheless, the assembly protocol for such probes is based on manually packing up the insulated wires with exposed tips. Although the MWAs have been utilized for decades, they nonetheless present some practical limitations. Firstly, to perform the multi-sites measurement, more electrodes need to be integrated. Since a wire could only hold one electrode, bundling up wires will result in an escalation of probe size that causes tissue damage during implantation. Secondly, most MWAs tend to be bent during implantation and splayed inside tissues over time. Such a tendency results in inaccurate recording locations and displacement of tissues. Lastly, the electrodes for MWAs are merely the portion of uninsulated wires, precise control of impedance will be problematic.

Recently, silicon has become the most commonly used material for neural probes not only because of its exellent mechanical and electrical properties but also due to its well-established micromachining techniques. Unlike microwire probes, silicon-based probes can accommodate multiple electrodes in a single probe shank. Furthermore, the position, pitch, and size of multiple electrodes can be precisely controlled in micron scale for better spatial resolution. Thus, with MEMS techniques, high density and highly integrated silicon-based probe arrays become attainable without compromising the small size [30]. The impedance is determined by the area of an electrode and the type of material that is used. Since the space for putting highly dense electrode arrays is restricted by the size of a probe, it is more essential to adopt appropriate material for low impedance.

The Michigan probe is one well-known example of silicon-based, and taper-shaped probe with multiple metal electrodes with accurate size and positioned in precise pitches. A typical Michigan probe has a thickness of 15-50 μm with 30-50 μm wide silicon shank [31]. The basic microfabrication flow based on a series of photolithography processes has been described in detail previously [32]. To thin down the bulk substrate to the required thickness, the boron-doped layer or buried oxide layer is used as a so-called etch stop layer [33-35]. The Michigan probe is the beginning of the concept and a foundation that provided numerous ideas for other groups (Fig. 1-1 (a)). NeuroNexus commercialized Michigan probes and provides highly customizable probes with various choices for electrode materials, the number of electrodes and the size of the probes. The performance has been proved to be reliable in both acute and chronic monitoring [36]. Fig. 1-1 (b) shows a neural probe from NeuroNexus.

Recently, Raducanu et al. from KU Leuven reported a high channel count CMOS active neural probe with 1344 recording sites and 12 reference sites [37]. As seen in Fig. 1-1 (c), the recording electrode and reference electrode have a dimension of 20 μm x 20 μm and 20 μm x 80 μm respectively, and they are densely arrayed on a 100 um wide, 8 mm long shank. To amplify the source signal, a specialized circuit was embedded under each electrode. Traditionally, the essential aspect that restricts the number of electrodes is that a majority portion of the shank space would be taken by metal traces. To overcome this limit, the time-division multiplexing technique has been adopted in their research to realize a highly compact electrode array.

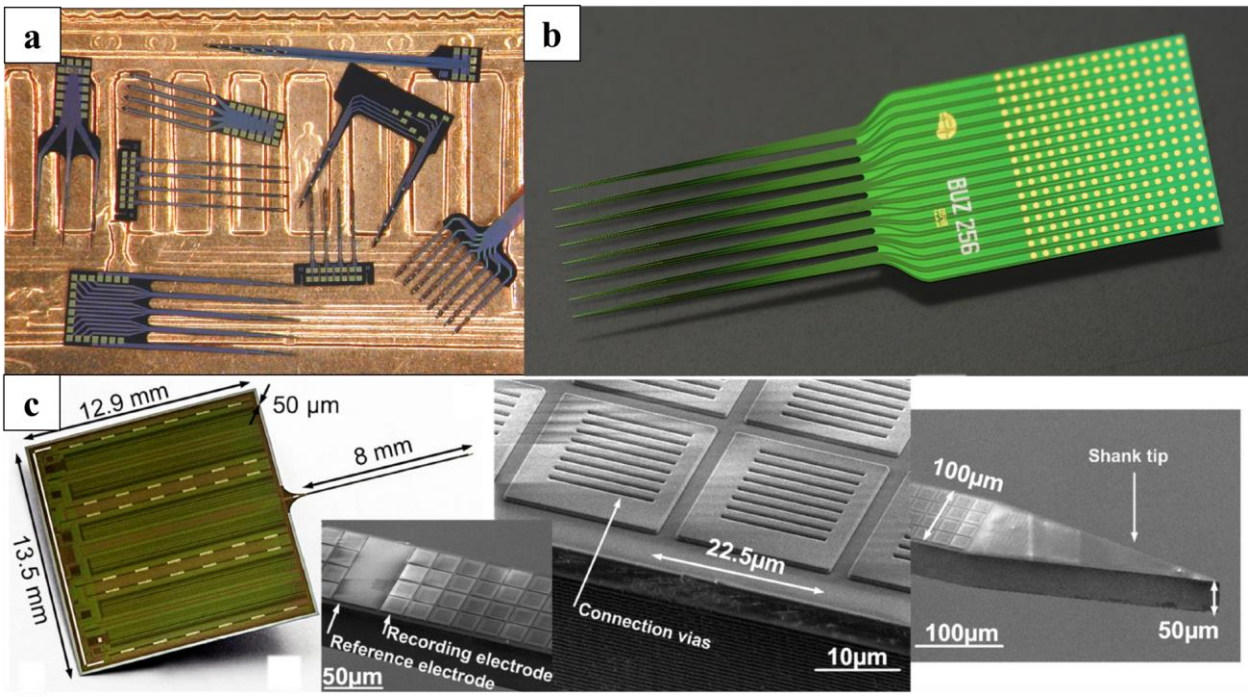

Figure 1-1. (a) Single-crystal silicon ribbon cables that introduced in Michigan in 1989 [32]. (b) A standard multi-shank probe from NeuroNexus by using MEMS technologies originally from the University of Michigan [36] (c) A time-division multiplexed neural probe with 1356 recording sites [37]

The primary issue for a silicon-based stiff probe is its mechanical mismatch with the soft brain tissue [38]. Recently, there has been an increasing interest in making soft probes. Studies have shown some advantages of flexible probes, including: 1) minimized tissue damage [39], 2) conformal contact with tissue, 3) lightweight and 4) low cost [40]. However, these benefits were accompanied by the intrinsic implantation difficulty due to the low Young's Modulus of soft materials. For this reason, early flexible probes were mainly designed to be used at the surface, or with a penetrating depth of a few millimeters. In order to reach deep brain structures, two typical methods are employed for most studies. The first one is achieved by coating a biodegradable layer of material to make the probe temporally stiff during implantation. Such materials that have been reported

include polyethylene glycol (PEG), maltose and sucrose gel [41-48]. The other attempt is to use a removable shuttle to reinforce the probe during implantation [49-52].

Traditionally used materials for flexible probes include polyimide, parylene, SU-8 and PDMS due to their biocompatibility and mechanical match with tissues which is essential for chronic implantation with minimal inflammation [39]. Mercanzini et al. presented a polyimide-based neural probe for cortical recording [53]. As shown in Fig. 1-2 (a), two layers of platinum electrodes are used to increase the number of recording sites without compromising probe size. As shown in Fig. 1-2 (b) Kim et al. reported a flexible neural probe based on hybrid silicon-parylene structure [54]. The locally flexible parylene portion was designed to reduce the mechanical mismatch between probe and tissues, and traditional implantation difficulty for polymer probes was also minimized due to the rigid silicon part. Xie et al. from Harvard University developed a three-dimensional macroporous nanoelectronic brain probe (Fig 1-2 (c)) that combines ultra-flexibility and subcellular feature sizes to overcome the limit of stability in chronic monitoring for silicon-based probes [55]. The microfabrication methods of stiff and polymer probes are generally similar. However, thanks to material properties, some creative structures are possible for polymer probes. Wu et al. from the University of Michigan reported a flexible fish-bone-shaped neural probe with biodegradable silk coating for implantation [56]. As shown in Fig. 1-2 (d), such design is beneficial for the minimum tissue reaction and has a large separation between the electrodes and shanks. The presented silk coating would be completely degraded within 30 minutes to 25 hours according to the condition of water annealing.

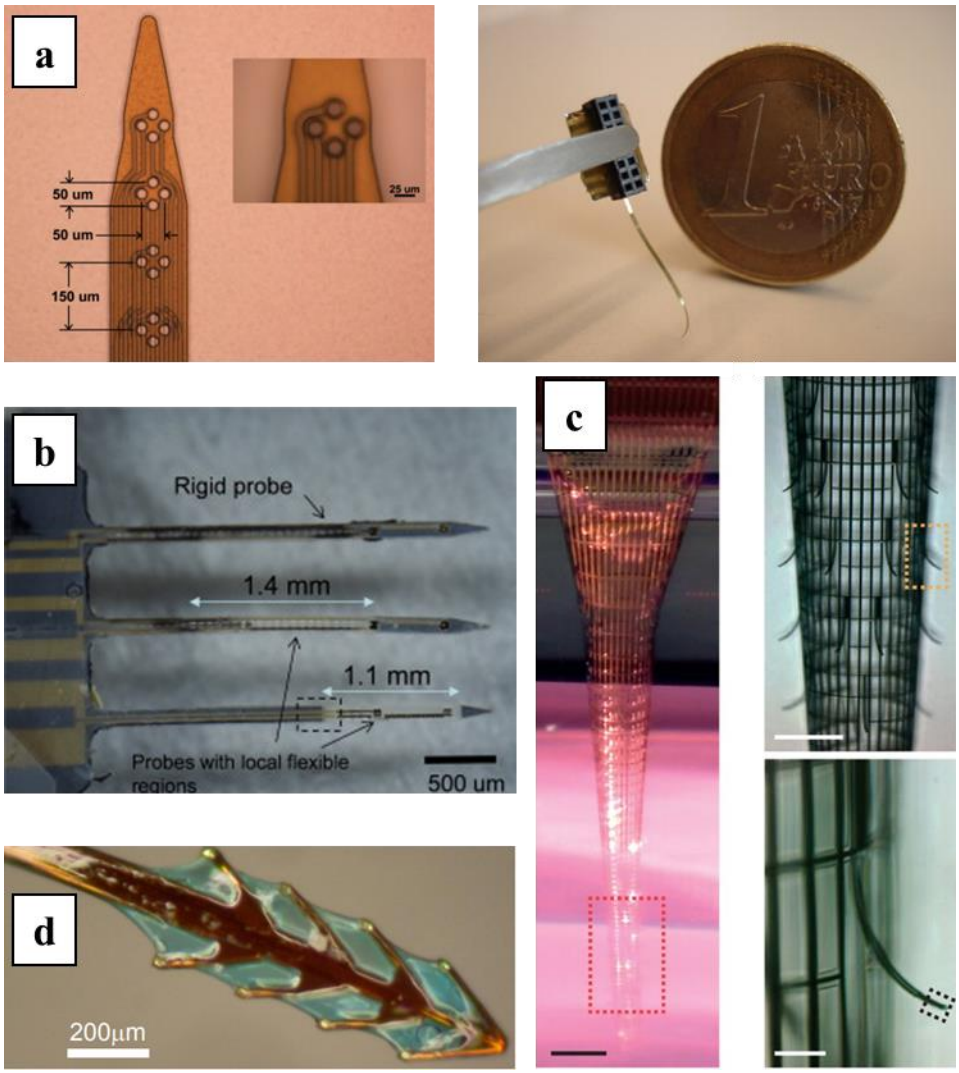

Figure 1-2. (a) Polyimide based neural probe for cortical recording [53] (b) a flexible neural probe based on hybrid silicon-parylene structure [54] (c) A three-dimensional macroporous nanoelectronics brain probe [55] (d) a flexible fish-bone-shaped neural probe with biodegradable silk coating for implantation [56]

One of the disadvantages of soft probes is that it couldn't withstand severe tissue environments such as spinal cord. To improve the mechanical property of soft probes, Kim et al. from Drexel University developed a braided multi-electrode probe. As seen in Fig. 1-3(a) – (c), the authors used up to 24 ultra-thin polyimide insulated nichrome wires interwoven into a tubular structure probe with multiple electrodes. It showed a 4 to 21 times improved mechanical compliance compares to a 50 μm nichrome wire [57]. In

addition, Do and Visell developed stretchable, twisted conductive microtubules by twisting two highly stretchable elastomer tubules. Each tubule was simply made by using a roller coating process along with a subsequent liquid conductor injection. Fig. 1-3 (d) and (e) show the method of constructing a woven electronics fabric by using twisted microtubules. Such a technique can be adopted in various applications such as human motion sensing, motion sensing for cable-driven robotic systems and stretchable electronics, etc [58].

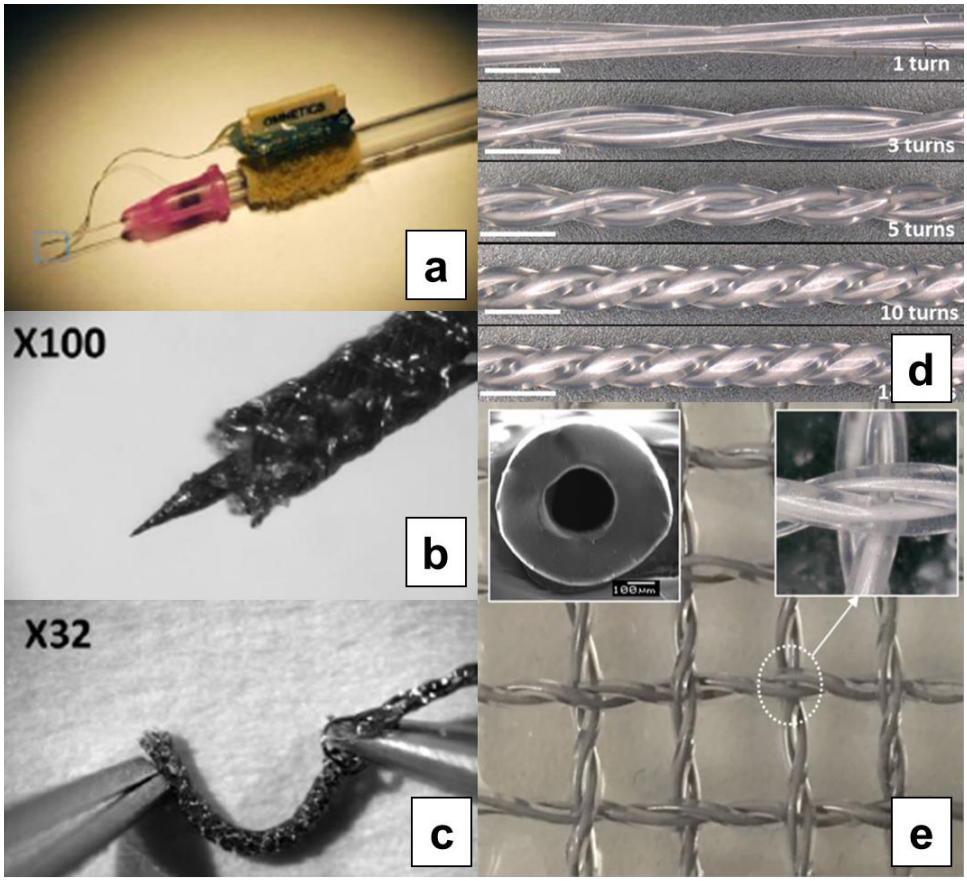

Figure 1-3. (a)-(c) Braided flexible multi-electrode probe [57]. (d) and (e) Different numbers of turns per twisted wires and woven electronics sensing fabric using twisted conductive microtubules [58].

For the last two decades, neural probes are becoming very versatile, providing functionalities more than just neural recording or stimulating. More advanced

multifunctional miniaturized probes have been developed by either integrating various electronic elements into the current structure or modifying the fabrication process. The representative applications are optogenetic [23] and drug delivery [24].

Optogenetics as a technique of neuromodulation takes advantage of photo-sensitive proteins expressed on a neuron cell membrane. Thus the targeted neuron could be activated or inhibited optically. There are two typical light delivery methods: (1) using built-in waveguide such as optic fibers with a laser illumination source and (2) integrating micro-LEDs directly on probes. LeChasseur et al. reported dual-core fiber optic-based microprobes [59]. As shown in Fig. 1-3 (a), the probe contained a hollow core that was filled with an electrolyte solution (1-3 M NaCl) to record electrical activity and an optical core which was a waveguide for collecting sufficient light efficiently to the tapered tip. A 488-nm laser was used to stimulate ChR2 and eYFP with pulses of light. Wu et al. reported a silicon neural probe by monolithically integrating recording sites and microscopic LEDs on the probe for optogenetic applications [60]. As shown in Fig. 1-3 (b), the μLEDs and recording sites were designed to be similar to pyramidal neuron soma and a total number of 12 μLEDs and 32 recording sites were on this four-shank probe. 60 nW power had been used for inducing spiking and fast population oscillations were induced in microwatts range. In addition, Kim et al. reported injectable, cellular-scale optoelectronics with applications for wireless optogenetics [61]. As shown in Fig. 1-3 (c), the polyimide-based flexible probes provide minimal damage to tissues and can be split into five different layers. Each layer has its own element: the first layer is Pt microelectrode; the second layer is silicon μ-IPD for optical measurement; the third layer

is μILEDs for optical stimulation; the fourth layer was a serpentine Pt resistor for temperature sensing; and the last layer was microfluidic channels for chemical delivery.

Integrating the drug delivery system to current miniaturized probes can address challenges that conventional drug delivery systems are confronting. A conventional drug delivery system such as oral or intravenous administration has limits for some of the modern drug candidates because of their large biomolecules with low bioavailability, and small therapeutic windows. Furthermore, some areas in a human body are very challenging to reach with conventional intravenous method because of the physical barrier that separates some organs from blood [24]. Lee et al. presented a multifunctional neural probe by combining a drug delivery system to realize chemical stimulation and individual neuron signal recording simultaneously [62]. As shown in Fig. 1-3 (d), a chemical outlet with a diameter of 60 μm and eight iridium electrodes with a dimension of 19 x 19 μm were included in a single probe. A constant air pressure controlled by an MFC (Mass Flow Controller) was used for a constant flow rate. A similar approach has also been reported by Petit-Pierre et al. As shown in Fig. 1-3 (f), the group reported a droplet-based microdialysis collection system by integrating a microfluidic channel into a neural recording and stimulation probe [63]. Furthermore, Liu et al. developed a silicon-parylene hybrid neural probe with microfluidic channel integrated as shown in Fig. 1-3 (e) [64]. The antibiotics were delivered through the microfluidic channels to reduce tissue inflammation, and such structure induced less tissue reaction comparing to the conventional neural probes.

Taken together, many MEMS-based probe techniques have been used for a variety of applications in neuroscience. Despite researchers have made tremendous efforts on

improving the performance of biomedical probes, many challenges have yet to be conquered due to the complexity of the neuron network of the human body. Thus, it is important to prioritize the desired features based on the specific applications when designing the device, and some of the functions can be compromised to strengthen other important ones. Our research aims to develop biomedical probes that are biocompatible, durable, reliable and multifunctional along with high sensitivity. In this dissertation, some of our recent works on how we attempt to achieve this aim will be discussed in detail.

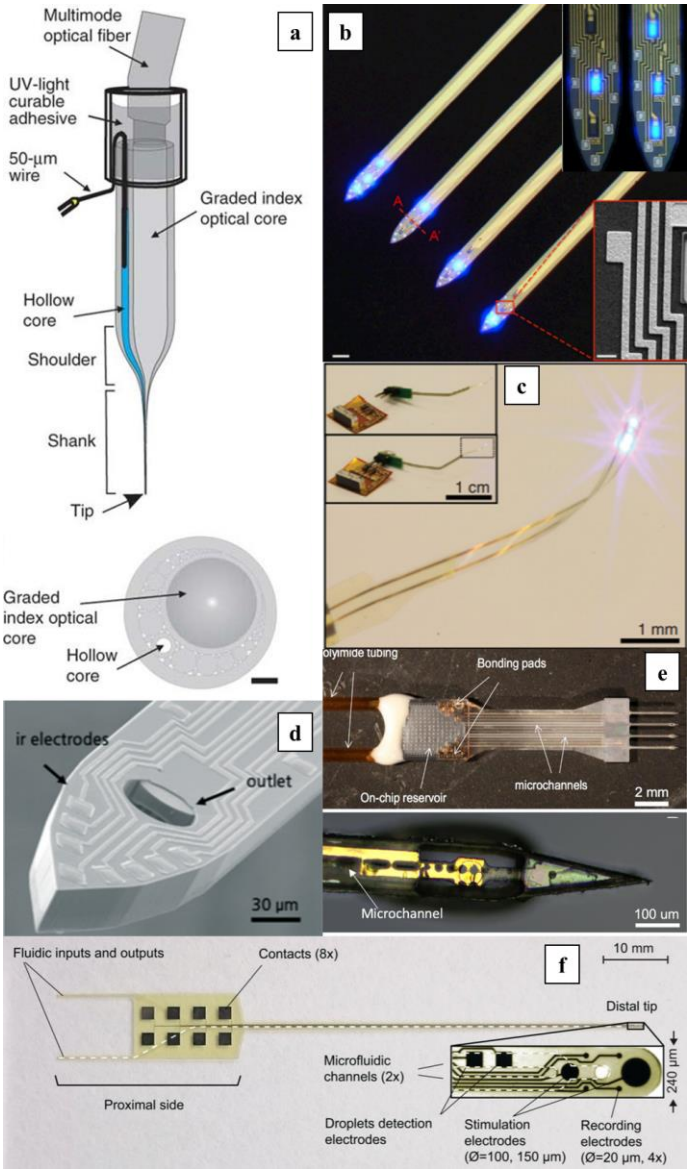

Figure 1-4. (a) A dual-core fiberoptic-based microprobes [59] (b) a silicon neural probes by monolithically integrating recording sites and µLED on the probe [60] (c) an injectable, cellular-scale optoelectronics with applications for wireless optogenetics [61] (d) a multifunctional neural probe with combining a drug delivery system [62] (e) a silicon-parylene hybrid neural probe with microfluidic channel integrated [64] (f) a droplet-based microdialysis collection system by integrating a microfluidic channel into a neural recording and stimulation probe [63]

Chapter 2 : General methods of microfabrication

As mentioned in the previous chapter, biomedical microprobes made from rigid and flexible substrates mostly share similar MEMS-based microfabrication processes that enable the precise patterning of miniaturized structure. In this chapter, the core processes for most of the fabrications in our work are outlined, and the basic operating principles of the tools are briefly described. In addition, the parameters along with the specific products that were used for each step are specified.

Photolithography

Most of the microfabrication processes start with photolithography, a technique that transfers the patterns from a designed mask onto a substrate such as a silicon wafer. Among alternative photolithography techniques, the one using UV as a light source is most widely used in modern IC and MEMS fabrication. Such a technique exploits a UV light source to expose photoresist thin film through a micropatterned photomask. The photoresist is mainly composed of a resin-based polymer, a sensitizer, and solvent. The structure of the polymer changes when exposed to the UV light, the sensitizer controls the chemical reaction, and the solvent enables a controllable thin layer using the spin coating system [65]. Generally, photoresists can be categorized into positive photoresist and negative photoresist.

For the positive photoresist, the UV exposed portion generates carboxylic acids that are soluble in the base chemical (called developer). The most frequently used positive photoresist is able to absorb from below 300 nm and up to 435 nm of UV light.

On the contrary, an exposed portion of the negative photoresist is crosslinked and becomes insoluble in the developer. One of the disadvantages of negative photoresist is

that the resolution is limited by the film thickness. This is because the cross-linking process needs to compete with polymerization, thus, the exposure time should be greater for thick resist than the thin resist to make it insoluble.

Depending on the pattern geometry, cost, speed and resolution requirements, etc., the photoresist tone will be chosen accordingly. In this work, feature sizes for most of the device designs range from a few microns and up to hundreds of microns. Positive photoresists have been employed for most of the processes because of the excellent plasma etch resistance. KEMLAB KL5310 was used for general exposures, and for the processes that need thick photoresist, AZ P4620 and DOW MEGAPOSIT SPR220-7 have been used. According to the minimum feature size of the work presented in the dissertation, mylar masks from FineLine Imaging in Colorado Springs, CO were used for most of processes.

Reactive Ion Etching

Reactive Ion Etching (RIE) is one of the methods of dry etching. It's widely used thanks to the properties that allow good vertical profile, dielectric etching, and high resolution. RIE is a physical-chemical etching, which is a method that combines the advantages of pure physical etching such as sputtering, and pure chemical etching such as plasma etching. An RIE etching chamber typically consists of two electrodes that create an RF electromagnetic field with a frequency of 13.56 MHz. The difference of an RIE system comparing to other dry etch systems is that the powered electrode is the cathode. The ionized gas species are attracted by the cathode and bombard at the surface of the sample, making the surface reactive for neutral gas plasma. It's worth noting that most of the etching in the RIE system is done by neutral radicals rather than

ion bombardment. When gases are introduced into the chamber, they are partially ionized in the RF power to generate the plasma and release free electrons simultaneously. Part of the free electrons is absorbed in the sample platter and build up negative charges that induce a DC bias between reactive species and samples (sheath area). Ions are accelerated due to the high electric field in the sheath area and strike to the samples, clear out the passivation layer on the surface of the samples or make the surface more reactive for neutral radicals.

In this work, RIE is the key process for most of the fabrications. Oxygen is mostly used for etching polymers like parylene and photoresist at a flow rate of 30 sccm. Carbon tetrafluoride (CF_4) in combinations with oxygen is used for silicon dioxide and silicon nitride etching. Sulfur hexafluoride (SF_6), butylene (C_4H_8), and Argon (Ar) are used for silicon deep etching. Detailed parameters will be presented in Chapter 3.

Deep Reactive Ion Etching

Deep Reactive Ion Etching (DRIE), as a subclass of RIE, has acted as an important role for etching silicon in this work. Deep RIE shares a similar system configuration as RIE. One thing that differentiates it from the RIE system is that the Deep RIE system has an even bigger anode electrode than RIE, which enables higher current density and sheath voltage. In addition, Deep RIE system operates through its unique process called Bosch process which provides a highly vertical sidewall profile by rapidly switching sulfur hexafluoride (SF_6), which is for isotropic etching of silicon, and octafluorocyclobutane (C_4F_8) which is used to form a passivation layer mainly on sidewalls to keep them from being etched, then remove the passivation layer at the bottom by Ar^+ sputtering. Literally, given an adequate feature size, DRIE can achieve as deep as hundreds of microns with

a vertical profile. By taking the benefits of these advantages, microfabricated elements, which are even irregularly arranged, can be readily released from wafers. Likewise, deep trenches, which are required by most of our work, can be formed easily. In this work, most of the DRIE process has been done by Plasma-Therm 970 SLR, and detailed parameters will be presented in Chapter 3.

Xenon Difluoride Silicon Isotropic Etching

Xenon difluoride (XeF_2) is known as a strong oxidizing agent, but in MEMS, it is particularly used as an etchant of silicon. XeF_2 etching of silicon is a spontaneous, non-plasma, pure chemical etching. XeF_2 etches silicon in every direction (isotropic) at room temperature under a certain pressure. It does not need any kinds of power to activate etchant or other agents. The whole etching process between silicon and XeF_2 is described as below:

$$2XeF_2 + Si \rightarrow 2Xe\ (g) + SiF_4\ (g)$$

The etch rate is somewhat fast in this reaction without any non-volatile byproducts and remaining residue. Thus the etching process is usually split into multiple cycles to ensure the exact target depth. In addition, XeF_2 has a high selectivity for silicon from the typical masking materials such as SiO_2 and photoresist. By taking these advantages and the nature of isotropic etching, a unique hollow parylene tube structure is developed and characterized. Detailed techniques and parameters will be discussed in Chapter 3.

Electron beam evaporation

Electron beam evaporation, as one of the methods of PVD (physical vapor deposition), is a commonly used process for metal deposition. In an electron beam evaporation system, electrons are either excited or extracted, depending on the source

type, from a tungsten filament and magnetically directed to the metal source in a low-pressure chamber. The electrons then strike the metal source, and when high enough energy is transferred during the collision, the metal melts and starts evaporating, being deposited on all surfaces of the chamber including the substrate. In this work, a model of BJD-1800 is used for most of the process. A combination of titanium and gold is used for electrodes, and aluminum is used for a metal mask. Other materials such as platinum will also be considered for future works.

Parylene Chemical Vapor Deposition

Parylene is a material that is chemically polymerized with Poly (P-xylylene). It is a generic name for some variants such as Parylene N, D, and C which show similar properties like dielectric and good moisture resistance. Nevertheless, with the different bonding materials, each of them has its own benefit in different applications. Parylene coating is a process of chemical vapor deposition. First, the precursor dimer is vaporized into a gaseous phase at 135 ºC, then the gas is pyrolyzed into monomeric gas after it goes through a furnace that is heated up to 690 ºC. Eventually, monomeric gas is condensed and deposited everywhere in the chamber at room temperature, and the coated Parylene thin film is highly uniform and conformal. In this work, Parylene C is employed by most of our devices due to its superb bio-compatibility and moisture barrier property. I make use of PDS2010 CVD machine of Specialty Coating Systems.

Chapter 3 A flexible Ag/AgCl micro reference electrode based on a parylene tube structure[1]

Introduction

Recently, there have been many efforts to develop miniaturized electrochemical sensors for microfluidic lab-on-chip analyses or in-vivo biological monitoring. The reference electrode is an essential component of electrochemical sensors and thus has received considerable attention [67]. The most widely used reference electrodes are Ag/AgCl (silver/silver chloride) electrodes, which are constructed by immersing a silver wire coated with AgCl in KCl (potassium chloride) or other Cl−ion-rich solution. The electrochemical reaction on the Ag/AgCl reference electrode is represented by the following equation:

$$AgCl\ (s) + \ e^{-} \leftrightarrow Ag\ (s) + Cl^{-}\ (aq)$$

Many micro reference electrodes have been developed based on this mechanism [67]. In some cases, the reference electrodes are simply thin-film Ag/AgCl electrodes without a filling solution [68]. They have the advantage of a simple microfabrication process. However, a disadvantage of a thin film Ag/AgCl is a short lifetime due to the small amount of Ag/AgCl. Furthermore, their potential is very sensitive to the testing solution due to the lack of a filling solution. Therefore, their application as reference electrodes is limited. To reduce the sensitivity of these electrodes to Cl^- ions and the pH value, Ag/AgCl films can be covered by gels filled with electrolytes. For example, Huang

---

[1] *Text and figures reprinted with permission from [66] E. Kim, H. Tu, C. Lv, H. Jiang, H. Yu, and Y. Xu, "A robust polymer microcable structure for flexible devices," Applied Physics Letters, vol. 102, no. 3, pp. 033506-033506-4, 2013.*

et al. used agarose gels filled with KCl, which function both as a solid internal electrolyte and an ion diffusion membrane [69]. Liao et al. mixed KCl with agar gel for the inner electrolyte and used chloroprene rubber for the liquid junction and insulator [70]. Due to the finite amount of Cl^-, these types of electrodes may still suffer from stability issues during long-term applications.

To make more stable reference electrodes, there have been a number of efforts to integrate a reservoir of KCl or other Cl^- ion rich solutions in these electrodes. Suzuki et al. developed a liquid-junction Ag/AgCl reference electrode with microfabrication techniques [71]. The solution reservoir was fabricated on a silicon substrate using anisotropic etching. In later work, this group formed the electrolyte layer by screen-printing a paste containing fine KCl powder and encapsulating it using silicone [72]. The electrolyte layer was then activated by injecting a solution saturated with KCl and AgCl.

The miniaturization of the reference electrode is a challenging task [67]. The lack of a reliable, long-lived reference electrode limits the performance of microelectrochemical sensors. Here we report a novel hybrid approach to developing a flexible microfabricated reference electrode with an internal electrolyte reservoir and a Ag/AgCl metal wire. This approach combines several advantages. Compared with thin films, a Ag/AgCl wire can provide large amounts of Ag and AgCl, preventing the failure of the electrode due to the consumption of Ag or AgCl. In addition, an internal electrolyte reservoir can lead to a stable reference voltage. Unlike its glass pipette counterparts, the flexibility makes this device very robust during application. In addition, its compatibility with microfabrication allows the integration of other components, leading to truly miniaturized electrochemical sensors or sensing systems.

Experiments

Design and fabrication process

The proposed reference electrode is schematically illustrated in Fig. 3-1. The reference electrode is formed by inserting a silver wire coated with a AgCl layer into a KCl filled parylene tube. Note that the central parylene tube is filled with electrolyte through one of the two side channels, whose inlets locate at ends of the two silicon beams. The tip of the tube is sealed with agarose gel saturated with KCl. For pH sensing, a pH indicating electrode is integrated on the top surface of the tube. The contact pad of this electrode is on the silicon pedestal, which also facilitates the handling and microfluidic coupling to the parylene tube.

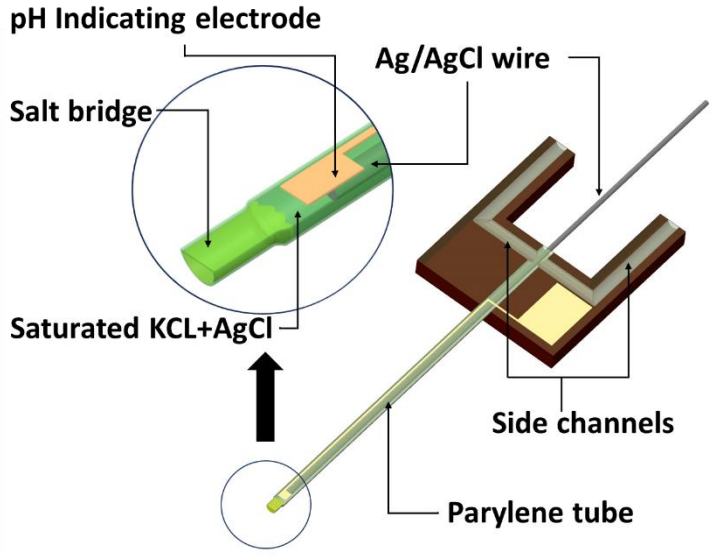

Figure 3-1. 3D schematic of the new reference electrode.

The fabrication process of parylene micro-tubes is based on XeF_2 isotropic etching and parylene conformal coating [22, 54, 73, 74]. The simplified process is summarized in Fig. 3-2. The left column shows cross-sections along the longitudinal direction of the parylene tube, whereas the right column shows the transverse direction. The fabrication

starts with the etching of 8 μm wide trenches into the silicon wafer using deep reactive ion etching (DRIE).

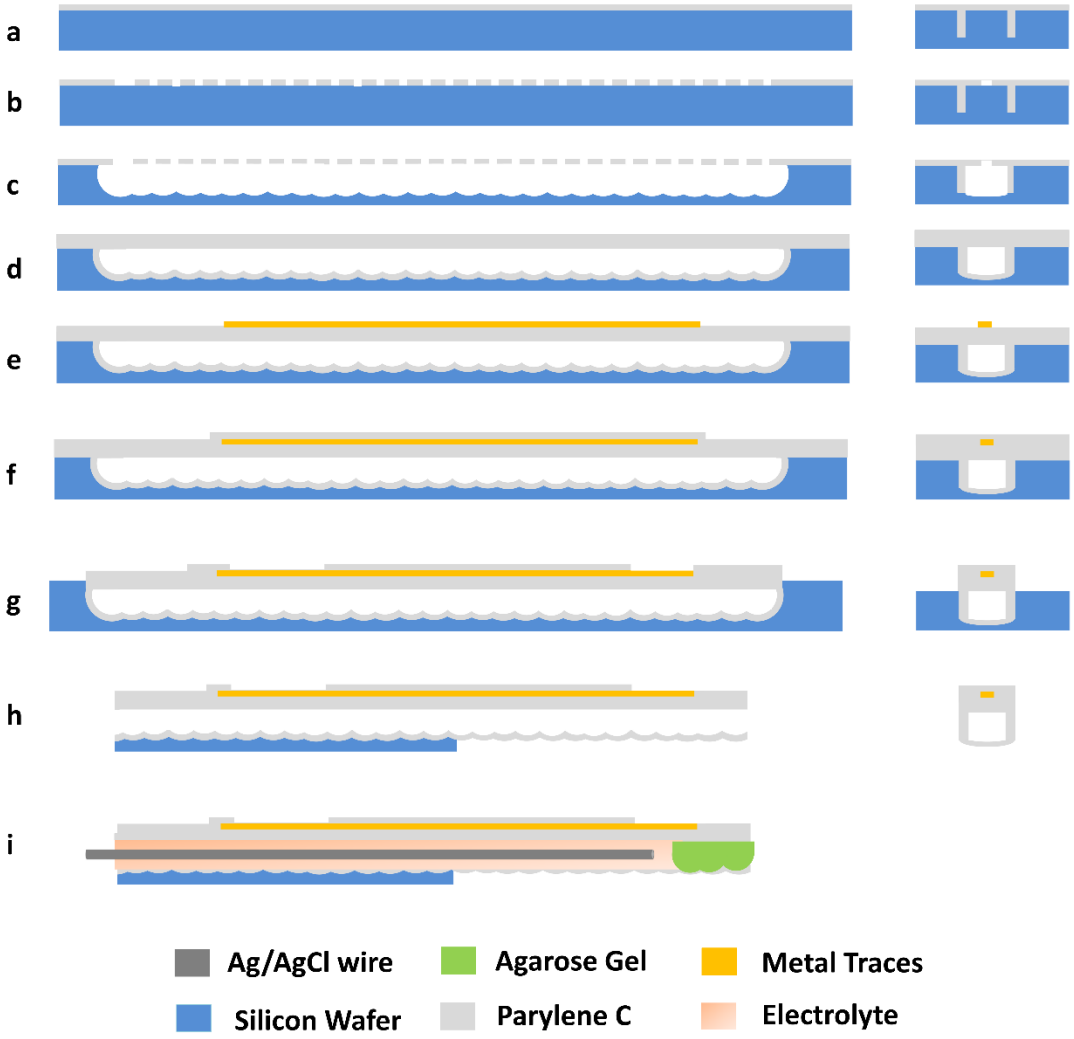

Figure 3-2. Simplified fabrication process: (a) Parylene C coating on a silicon wafer; (b) Patterning discontinuous holes on parylene; (c) XeF2 etching to completely undercut the handling wafer and form underlying channels; (d) 2nd parylene deposition to seal the previously opened parylene windows; (e) Ti/Au deposition to form electrodes/traces/pads; (f) 3rd parylene layer to insulate the metal layer; (g) Patterning the parylene layer; (h) Backside DRIE etching to release the device from silicon wafer; and (i) Insertion of the Ag/AgCl wire and sealing of the tip with agarose gel.

Subsequently, parylene-C is deposited onto the surface of the silicon by chemical vapor deposition (CVD). Thanks to the conformal deposition of parylene, deep trenches

will be refilled as shown in Fig. 3-2 (a). The resulting parylene structures in trenches form sidewalls for microchannels and barb structures in the salt bridge region to mechanically anchor the cured agarose gel. In the next step shown in Fig. 3-2 (b), parylene is patterned using an Al mask and oxygen reactive ion etching (RIE) to form discontinuous 8 μm x 20 μm holes that expose the silicon wafer. Then a gas phase etchant known as XeF_2 is used to etch silicon beneath the holes. Since this etch is isotropic, the silicon becomes undercut, and eventually, the cavities formed around each hole join to form a single continuous groove. A second deposition of parylene greater than 4 μm, shown in Fig. 3-2 (d) serves to coat the walls of the XeF_2 etched groove with parylene and seal the XeF_2 etch holes in the surface. This creates a sealed, continuous microchannel buried beneath the silicon. Next, as shown in Fig. 3-2 (e), a titanium/gold thin film layer of 250 nm is deposited by electron beam evaporation and patterned to form the shapes of microelectrodes, contact pads, and traces. These metal structures are insulated by the third layer of parylene 3 μm thick, which is subsequently patterned to expose electrodes and contact pads, as shown in Fig. 3-2 (f) and (g). During this etching, excess parylene around the device is also removed. Finally, as shown in Fig. 3-2 (h), silicon is patterned by backside DRIE, removing silicon from parylene structures intended to be free-standing, as well as shaping the silicon parts of the device. Assembly is completed with the insertion of an Ag/AgCl wire into the microchannel, loading of the electrolyte solution, and pulling of the agarose gel into the tip of the tube.

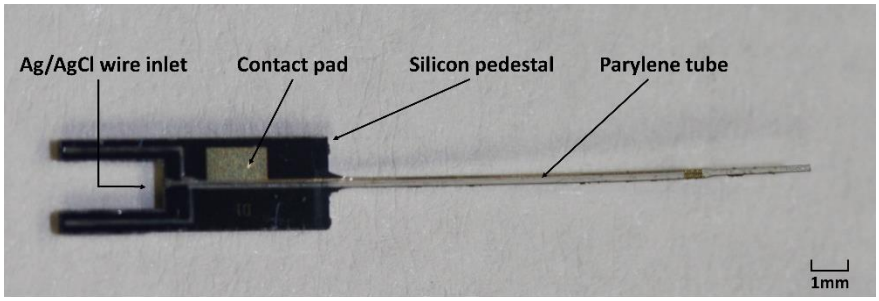

Figure 3-3. Prototype of a fabricated reference electrode.

Fig. 3-3 shows a fabricated device. The parylene tube is around 17.3 mm long. The initial width of the tube is 342 μm and it narrows down to 237 μm at the distal end. The magnified view of the distal end of the device is shown in Fig. 3-4, where the pH indicating electrode, arrays of sealed etching holes, and the transition from wide to narrow tubes can be clearly observed.

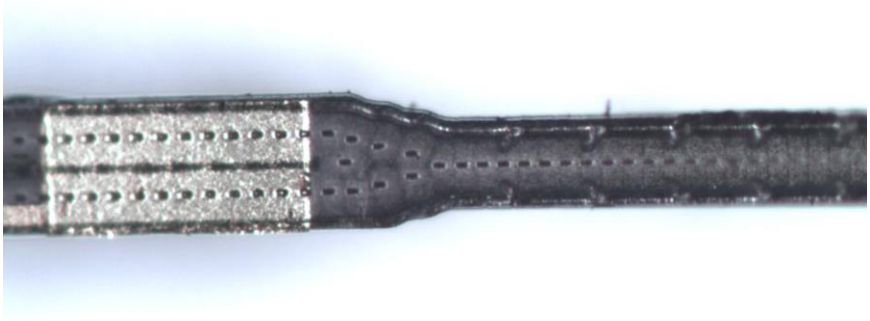

Figure 3-4. The distal end of the parylene tube.

The narrow tube is achieved by converging two rows of parylene windows into a single row for XeF_2 etching. The length of the salt bridge area can be adjusted to get an appropriate impedance. Fig. 3-5 (a) and (b) show SEM images of the overall device and

a cross-sectional view of the parylene tip, respectively. The parylene tube can be easily bent without causing any damage as illustrated in Fig. 3-6.

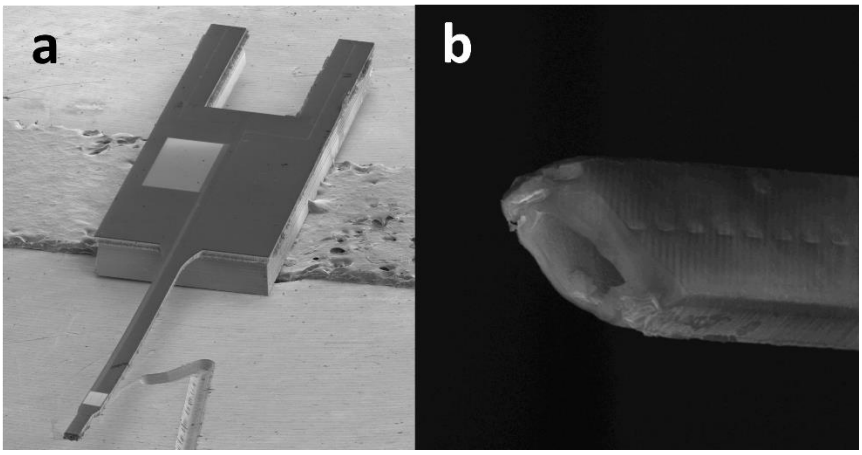

Figure 3-5. a) SEM image of an overall view of the reference electrode. b) SEM cross-sectional view of the parylene tip.

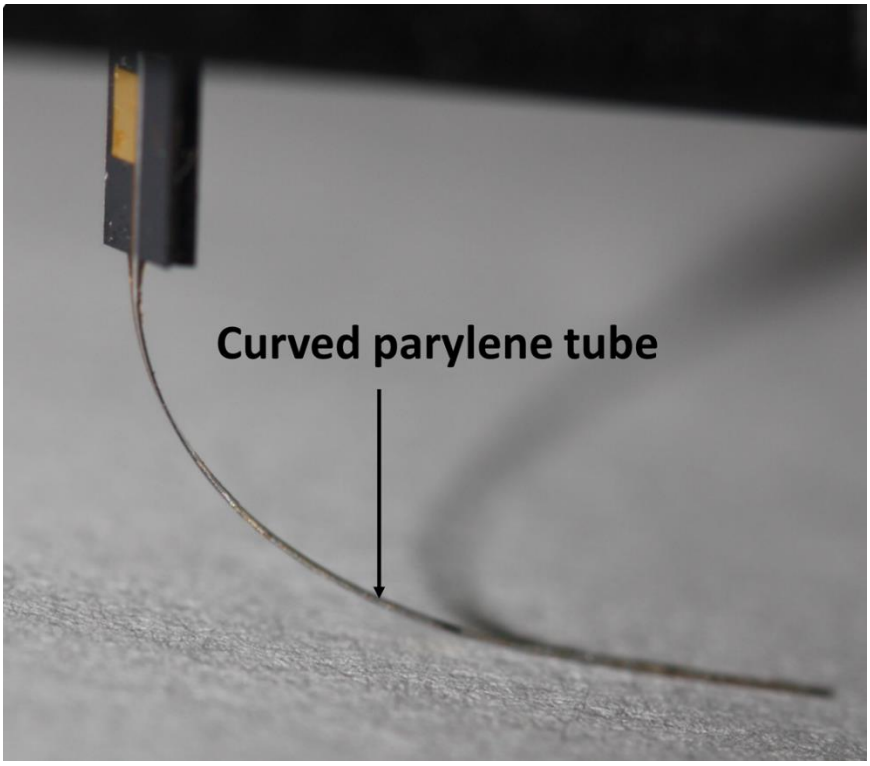

Figure 3-6. A curved parylene tube illustrating its flexibility.

A silver wire with a 50 μm diameter is chosen for the reference electrode. This diameter allows the formation of a thick AgCl layer while retaining sufficient Ag, preventing the failure of the device due to the limited amount of Ag or AgCl. A simple electrochemical method is used to convert Ag to AgCl. Note that an appropriate ratio of silver and silver chloride is important for good stability and reproducibility. To achieve optimal performance, 10–25% of silver should be converted to silver chloride according to [75]. In our experiment, a constant voltage of 500 mV is applied between an Ag wire and a large Pt electrode in a 1 M KCl solution for one hour. Fig. 3-7 plots the current as a function of time during AgCl growth. A drastic initial current rise can be observed at the start of the reaction, and it drops rapidly and saturates after the Ag surface is completely covered by the AgCl film. From the current, the total number of electrons that took part in the reaction is 5.66×10^{17}. From Eq. (1), it can be observed that the generation of one AgCl molecule is accompanied by the transfer of one electron. Therefore, the amount of AgCl created is 9.4×10^{-7} mol or 1.347×10^{-4} grams. For a 2 cm long Ag wire with a 50 μm diameter, 24 % of Ag was converted, leading to a 7.4 μm thick AgCl film.

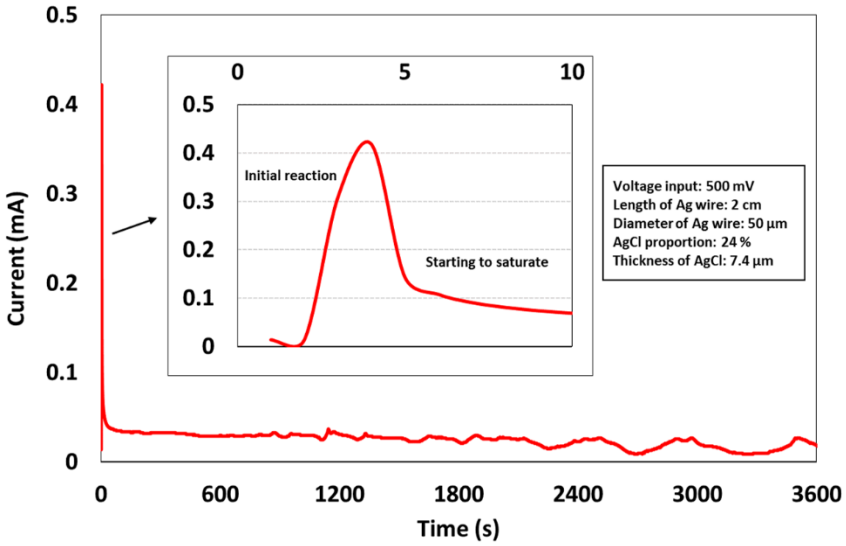

Figure 3-7. Current during AgCl electrochemical growth.

To assemble the reference electrode, a Ag/AgCl wire was first inserted into the parylene tube from the opening at the edge of the silicon interface chip. Since both the channel and wire are on a micro scale, this work was performed under a microscope with a pair of fine tweezers. Once the Ag/AgCl wire reached the other end of the channel, it was stopped because of the smaller size of the salt bridge area as illustrated in Fig. 3-4. The Ag/AgCl wire was fixed by applying a small amount of marine epoxy at the tube inlet on the silicon pedestal. Then the inner electrolyte, saturated KCl and AgCl solution, was injected into the parylene tube using a syringe through one of the polyimide tubes glued on the two silicon beams. Note that both silicon beams host a microfluidic inlet to the parylene tube. When electrolyte was injected through one polyimide tube, the other was sealed. During this process, the device was carefully observed under a microscope to avoid air bubbles inside the tube. Next, the smaller parylene tube at the distal tip was filled with 2% agarose gel saturated with KCl, which functions as the salt bridge of the reference electrode [76]. It was achieved by applying negative pressure to the syringe

on the polyimide tube, while the probe tip was dipped into an agarose solution. The temperature of the agarose solution was kept above 80 ºC during drawing to keep it in the liquid phase. The agarose solution inside the tube tip gelled quickly after the probe was removed from the hot solution. The agarose gel column is about 3 mm long. Finally, to avoid the inner aqueous electrolyte solution from evaporating, the end of the polyimide tube was sealed by epoxy. In order to maintain the integrity of the gel, the assembled device is stored in a saturated KCl solution.

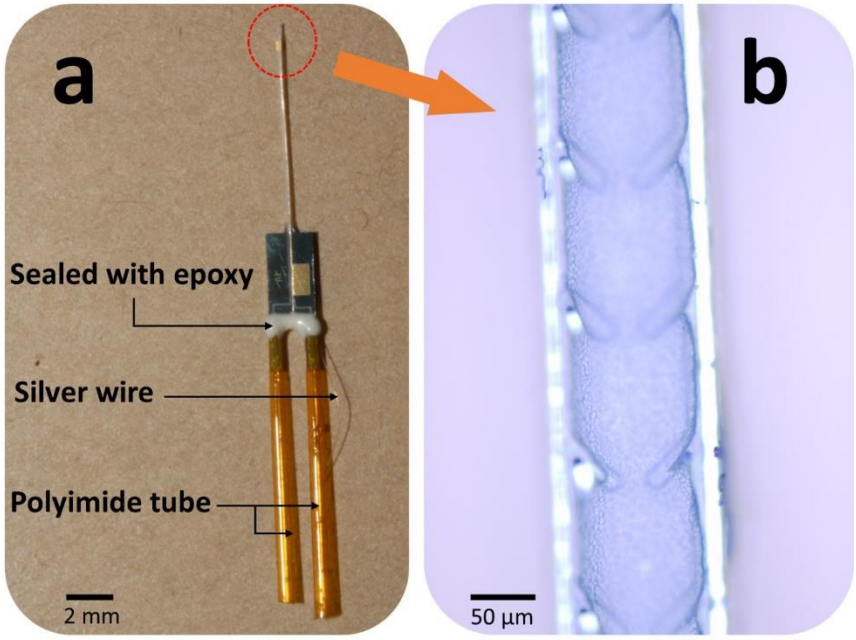

Figure 3-8. a) Prototype of an assembled reference electrode. b) Salt bridge area with barb structures.

An assembled micro-reference electrode is presented in Fig. 3-8 (a). Polyimide tubing is used here for the injection of the inner electrolyte and the drawing of the agarose gel to form the salt bridge as discussed previously. In order to mechanically anchor the gel, barb structures are implemented inside the tube as shown in Fig. 3-8 (b).

Characterization

We measured the potential difference between our electrode and a commercial reference electrode in 1X phosphate-buffered saline (PBS) solution, DI water and three different pH solutions as shown in Fig. 3-9. The commercial reference electrode is a LowProfile Ag/AgCl gel electrode (3.5 mm OD) from PINE Research Instrumentation, which is filled with 4 M KCl gel and has a typical variance of ±3–5 mV. The pH buffer solutions were purchased from EMD, and have pH values of 4, 7, and 10, respectively. The test started with a 1X PBS solution by connecting two reference electrodes to an electrometer (Keithley 6514). The voltage difference between the two electrodes was stable at around -36 mV for the duration of a 10-h experiment. Then, after a quick rinse, the test solution was changed to a pH 4 solution and monitored for another 10 h. The voltage difference was still stable at around -35 mV. Then the device was tested in pH 7 and pH 10 solutions, respectively. We observed that for devices immersed in PBS 1X and pH buffers at 4, 7 and 10, the maximum deviation of the average voltage recorded over at least 10 h was no more than 5 mV between solutions. In addition, the maximum variation of the recorded voltage over 10 h for each solution is less than 2 mV. The device has also been tested in DI water. As can be observed, the output is less stable than in other cases. However, the overall drift over the testing period is less than 5 mV.

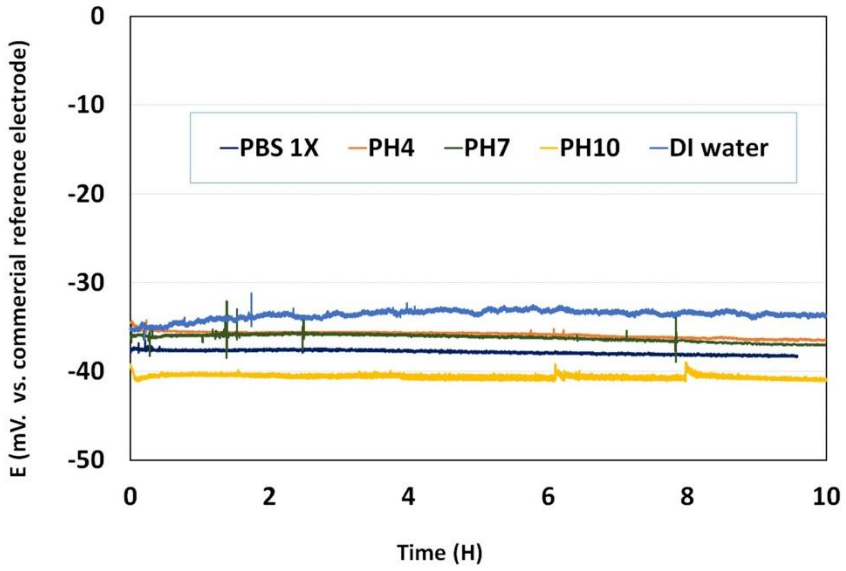

Figure 3-9. The potential difference between our reference electrode and a commercial reference electrode in different solutions.

Our device has been tested in KCl solutions with different concentrations and the results are plotted in Fig. 3-10. It can be observed that our reference electrode is insensitive to KCl concentration due to the internal electrolyte reservoir. The potential variation is less than 3 mV for KCl concentrations ranging from 0.1 M to 2 M.

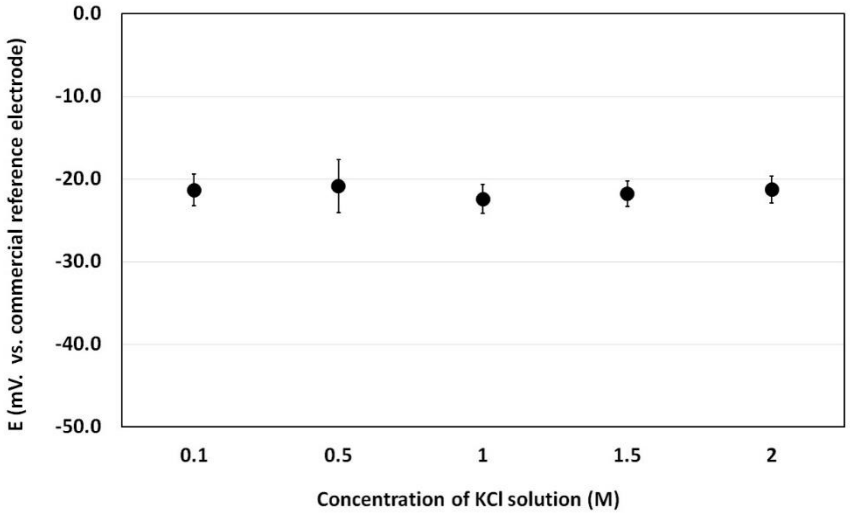

Figure 3-10. The potential difference between our reference electrode and a commercial reference electrode in KCl solutions with different concentrations. The average value and standard deviation are calculated based on a one-hour measurement.

The impedance of the new reference electrode has been characterized from 200 Hz to 20000 Hz with an LCR meter (HEWLETT PACKARD 4284A). The measured impedance is mainly resistive and approximately 60 kΩ, similar to the commercial reference electrode whose resistive impedance is around 1.5 kΩ.

To further investigate the response to pH, we combined our reference electrode with a glass-based commercial pH indicating electrode (Orion 350 PerpHect Meters, Thermo) and measured their voltage in different pH solutions. A sensitivity of -54.6 mV/pH is obtained, close to the ideal Nernstian slope of -59.19 mV/pH [75].

In our experiment, the overall operation time of the tested device has exceeded 100 h. Note the operation time and stability of the reference electrode are affected by multiple factors such as the amounts of Ag/AgCl and Cl^- in the electrolyte. Many micro reference electrodes have a shorter operation time compared to their macro counterparts because the limited AgCl can be rapidly consumed due to the reduction of Cl ions in the

electrolyte [68]. To obtain a long operation time and stable reading for the reference electrode, we use Ag/AgCl wire instead of a thin film and integrate an internal electrolyte reservoir.

Our current device utilizes a 50 μm diameter Ag wire of which 24% is converted to AgCl. In the future, we plan to use thicker Ag wires, i.e., 75 μm. We will also integrate a larger reservoir on the silicon base in the next generation devices to significantly increase the electrolyte volume. It is also worth noting that the current reference electrode needs to be stored in a saturated KCl solution, in a way similar to commercial ones. This not only keeps a sufficient Cl^- concentration but also prevents the gel from dehydration.

A miniaturized pH sensor based on the reference electrode

To prove our approach can lead to miniaturized electrochemical sensors, a pH sensor has been demonstrated. The pH indicating electrode is formed by electrochemically depositing iridium oxide on the integrated gold electrode on the parylene tube surface. The electro-deposition was performed using a Princeton Applied Research Potentiostat/Galvanicstat Model 273A by sweeping a positive bias between 0 and 0.575 V (versus Ag/AgCl) at 50 mV/s for 50 cycles first, which enables the deposition of the high-quality thin film. Then a second pulse of 1 Hz between 0 and 0.575 V was performed for 3200 iterations [77]. The impedance has been measured in 1X phosphate-buffered saline (PBS) solution (a physiologically pH buffered solution with isotonic sodium chloride) through an LCR meter (HEWLETT PACKARD 4284A) shown in Fig. 3-11. The frequency range was set from 200 to 20000 Hz in 200 increments, and the voltage applied was set to 10 mV.

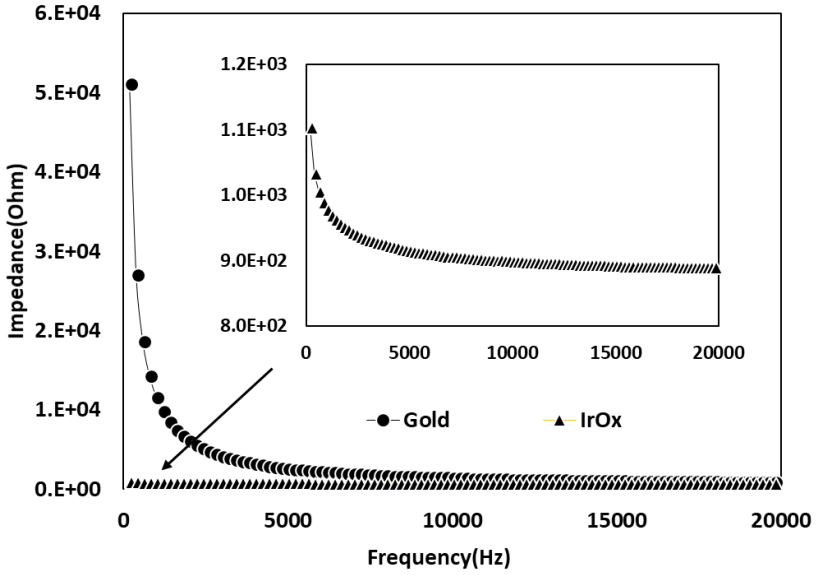

Figure 3-11. The impedance before and after IrOx coating.

To evaluate the IrOx as a working electrode, we first characterized it by measuring the voltage difference with a commercial reference electrode (LowProfile Ag/AgCl gel electrode,3.5 mm OD from PINE Research Instrumentation) as shown in the Fig. 3-12 (a), (b). A sensitivity of -65.06 mV/pH was obtained at 23 ºC.

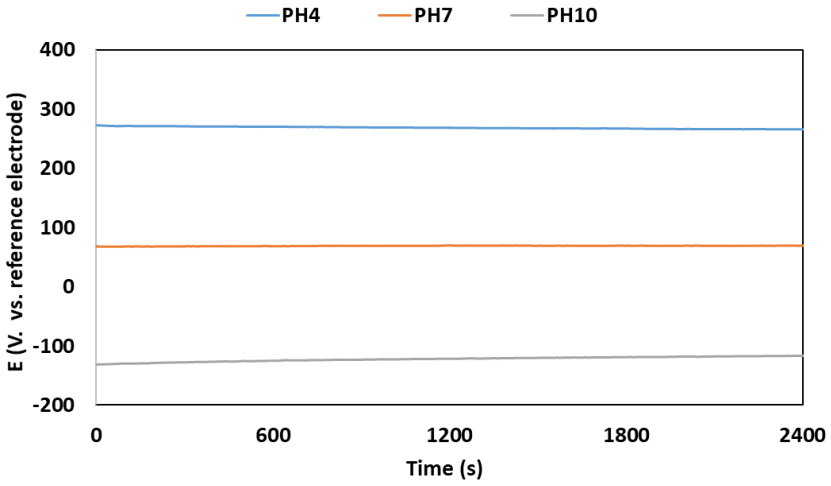

(a)

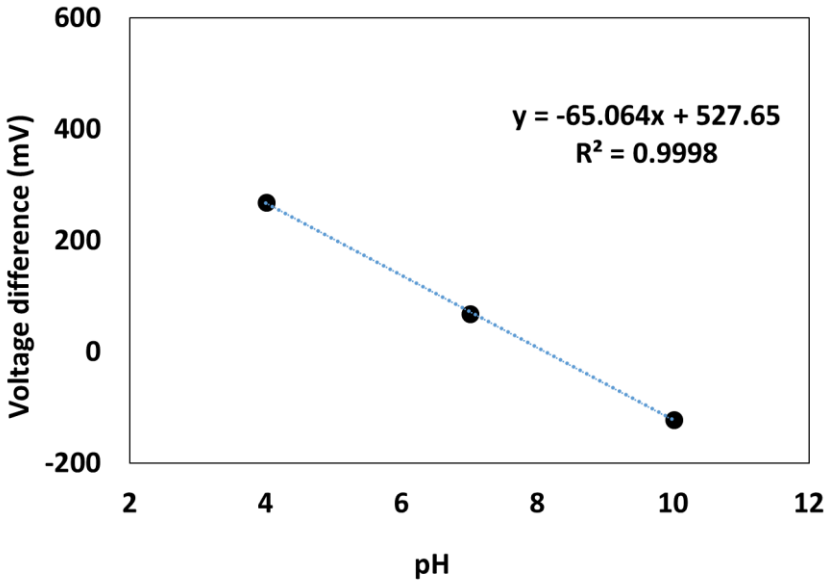

(b)

Figure 3-12. (a) The voltage difference of our IrOx versus commercial reference electrode in three pH buffer solutions. (b) Sensitivity measured in compliance with the result of (a).

On the other hand, We also characterized the pH sensor by measuring the voltage difference between our reference electrode and the integrated pH indicating electrode in three different pH buffer solutions for one hour. The results are plotted in Figure 3-13 (a). The drift over the one-hour period is between -5 mV and -10 mV, which is moderate compared to those observed by others [78, 79]. This drift is probably caused by different diffusion rates of anions and cations [79]. As shown in Fig. 3-13 (b), a sensitivity of -66.5 mV/pH was obtained with our pH indicating electrode, slightly larger than the ideal Nernstian slope of -59.16 mV/pH. It has been reported that activated iridium oxide (AIROF) and electrodeposited iridium oxide (EIROF) typically exhibits a sensitivity from -60 mV/pH to -70 mV/pH [78, 80, 81]. Therefore, our miniaturized sensor has a sensitivity that matches reported values in the literature.

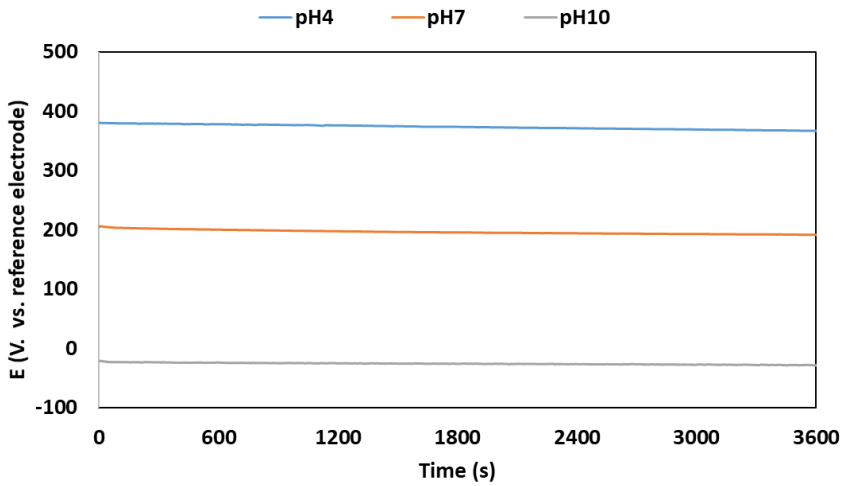

(a)

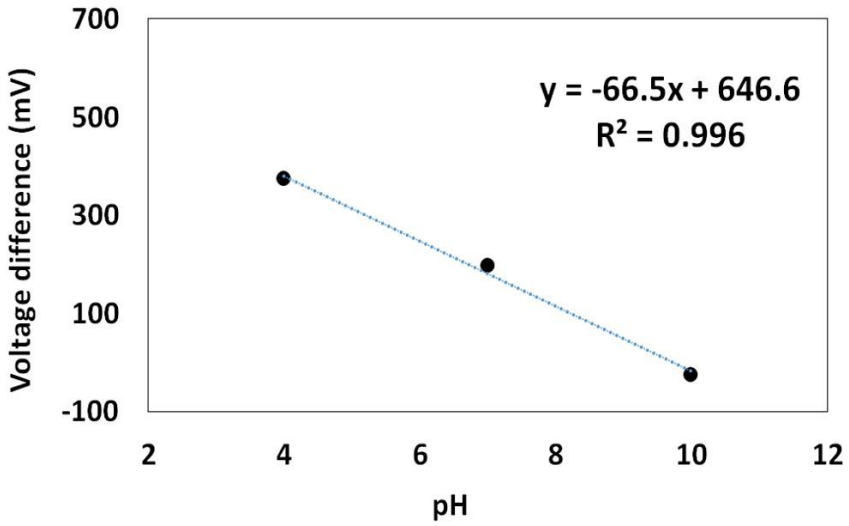

(b)

Figure 3-13. (a) The voltage difference of our IrOx versus our reference electrode in three pH buffer solutions. (b) Sensitivity measured in compliance with the result of (a).

Conclusion

A novel flexible microfabricated reference electrode has been successfully developed. By taking advantage of a unique parylene tube structure, we successfully integrated a Ag/AgCl wire and a reservoir for the inner electrolyte, leading to a long operational life and stable output. Compared to reference electrodes based on glass

capillaries, the flexible parylene tube makes the new electrode more robust. Our novel micro-reference electrode exhibited good stability in PBS and pH buffer solutions with a drift of 1-2 mV over 10 h. When the pH value is increased from 4 to 10, the voltage variation is less than 5 mV. The device has exceeded 100 operational hours without significant deviation from that observed with a commercial Ag/AgCl reference electrode. By combining a monolithically integrated IrOx pH indicating electrode, a miniaturized pH sensor has been demonstrated. This MEMS-based flexible reference electrode will be useful for 3D cell culture monitoring, in vivo electrochemical sensing, or other applications that request miniaturized electrochemical sensors.

Chapter 4 Flexible deep brain neural probes based on a parylene tube structure[2]

Introduction

A large variety of silicon neural probes have been developed using micromachining techniques to precisely form microneedles that carry thin-film microelectrodes [82-85]. Numerous groups are also attempting to make probes flexible to reduce the stress caused by the micromotions of brain tissues [86]. Polymers such as parylene, polyimide and SU-8 are widely investigated as flexible neural probe materials due to their good biocompatibility and microfabrication compatibility [41, 87-90]. Meanwhile, most of the microneedle probes have limited length, and thus are not able to reach many deep brain structures and brains of large animals. The main challenge is that ultra-long shanks may buckle or fracture during implantation. One simple way to increase the mechanical strength of ultra-long shanks is to increase the lateral dimension. For instance, Hajj-Hassan et al. [91] fabricated 10.5 mm long silicon shanks with a thickness of 50 μm and a width tapering from 150 μm to 50 μm. Ultra-long silicon probes with integrated microchannels have been developed as well by Fekete and others [92, 93]. Successful in vivo animal tests have been demonstrated using these multi-functional deep brain probes [94, 95]. The fracture of ultra-long silicon probes with integrated microchannels has also been studied [92]. Alternatively, the strength of the ultra-long shanks can be enhanced by attaching another mechanical supporter, either permanently or temporarily. NeuroNexus® developed deep brain probes by inserting silicon shanks inside a stainless steel tube (315–400 μm OD) permanently [96]. Plexon® also developed ultra-long probes

---

by manually assembling metal wires along half-opened metal tubes [97]. Pothof et al developed deep probes by wrapping polyimide foils with electrodes into 0.8 mm diameter cylinders and fill the hollow cylinders with epoxy [98]. Removable rigid insertion shuttles have been used to strength soft polymer probes during implantation [49-52]. In addition, polymer probes have been coated or injected with dissolvable or degradable materials such as polyethylene glycol (PEG), maltose and sucrose gel [41-48]. Moreover, silk coating has proven to be a reliable strategy for probe insertion due to its good mechanical and biodegradable properties [99, 100].

Here we report a new type of ultra-long neural probes based on a unique parylene tube structure. The 3D schematic in Fig. 4-1 shows the basic design of a single-shank ultra-long deep brain probe. The shank body is made of a hollow parylene tube. During implantation, metal wire can be inserted into the tube to reinforce the shank and strengthen it for insertion into neural tissue. The distal tip of the parylene tube can be either open or closed. When the tip is open, the protruding metal needle can facilitate the piercing of tough brain tissues such as the dura mater. The metal wire can be easily removed after implantation, leaving only the parylene shank in the brain tissue. Potentially, the flexibility of the parylene shank can minimize the stress caused by the micromotions of brain tissues and improves chronic stability responses [50, 101-107]. The inlet of the tube is located at the proximal edge of the silicon island. For the proof-of-concept purpose, the design is a single-shank device that has four electrodes. However, there are no fundamental obstacles that prevent developing multi-shank devices with high-density electrodes.

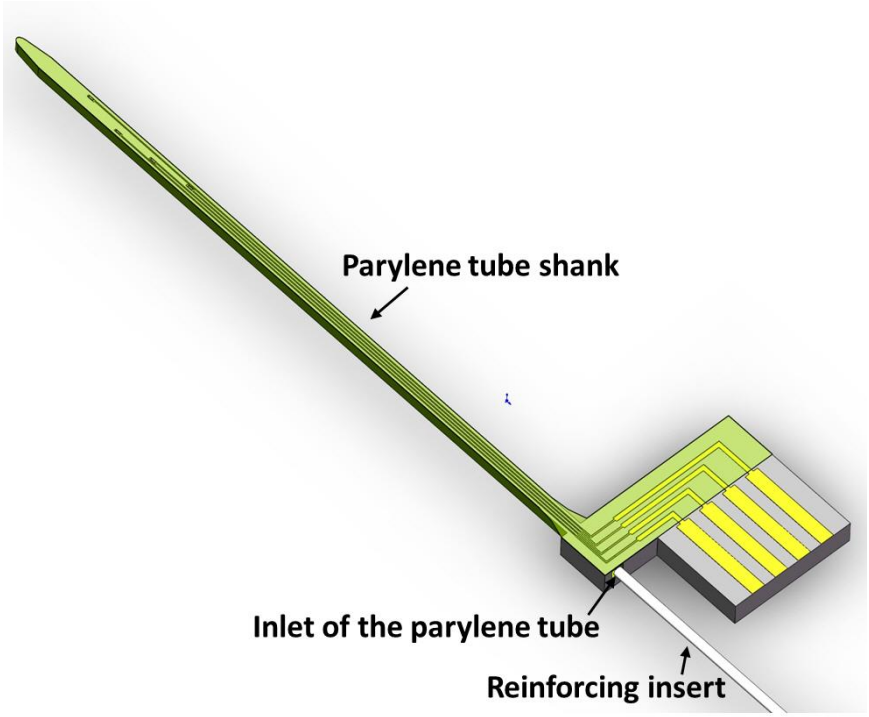

Figure 4-1. 3D schematic showing the concept design of the super long neural probe reinforced with an insert. In this diagram, green is parylene, yellow is gold, and gray is silicon.

Materials and Methods

Microfabrication and assembly

The microfabrication is based on a well-established process we demonstrated in our previous work [22, 54, 77, 108, 109]. Similar microchannel fabrication methods based on isotropic etching and sealing with polysilicon or SiO_2 have been reported by other groups to integrate the microfluidic capability to neural probes [110, 111]. The process flow, including both cross-sectional views and 3D schematics, is illustrated in Fig. 4-2. To start, a 300 μm silicon wafer was thermally oxidized and the resulting oxide layer was patterned at parylene tube area. Then a Ti/Au/Ti layer with a thickness of 20/250/20 nm was evaporated and patterned to form electrodes, interconnects, and contact pads. The second titanium layer serves to enhance the adhesion to the following parylene layer, and

it will be chemically removed later to release the gold electrodes. Note that the oxide was removed at parylene tube area to avoid cracking, but remained underneath bonding pads, as shown in the 3D schematic. Then DRIE (Plasmatherm SLR-770) was used to form 130-140 μm deep and 10 μm wide trenches on the silicon substrate. The standard Bosch process was used, with the process periods of 5 s, 2 s, and 6 s for passivation layer deposition, etch A (Ar sputtering) and etch B (SF6 plasma etching), respectively. The average etch rate was 0.5 μm/loop. These trenches were subsequently refilled by 5 μm vapor-phase deposited parylene C (PDS2010, Specialty Coating System), forming the sidewalls of the parylene tube. Windows with a dimension of 20 μm × 8 μm on the parylene layer were opened using oxygen reactive ion etching (200 mTorr and 200 W) with an aluminum mask. Next, silicon between parylene walls was completed etched away by XeF_2, a gas phase silicon etchant. The XeF_2 silicon etching was performed using a pulse mode. For every pulse, the XeF_2 vapor filled the etch chamber (800 mTorr), etched the silicon sample for 2 min, and was pumped away. The transverse dimension of the etched channel was controlled to be 140 μm × 140 μm. A total number of 50 etch cycles was performed to reach the target depth. Note the etch rate is mass-transport limited and a function of etch depth and exposed silicon area. Frequent inspection and measurement under the microscope are required to control the etch depth accurately. Due to the isotropic nature, XeF_2 etching through a 1D array of discrete parylene windows results in a continuous channel in the silicon substrate. The parylene sidewalls, previously defined by DRIE etching and refilled by parylene, serve to limit the lateral extent of the XeF_2 silicon etch. Next, a second 7 μm parylene C layer is deposited. Due to the conformal nature, this parylene layer deposited inside the silicon channel and sealed the parylene windows,

resulting in a closed continuous parylene tube. In the next step, oxygen plasma was carried out to expose the electrodes and bonding pads, and define the lateral shape of the parylene tube. Finally, DRIE was carried out from the backside to release the parylene tube and define the silicon base.

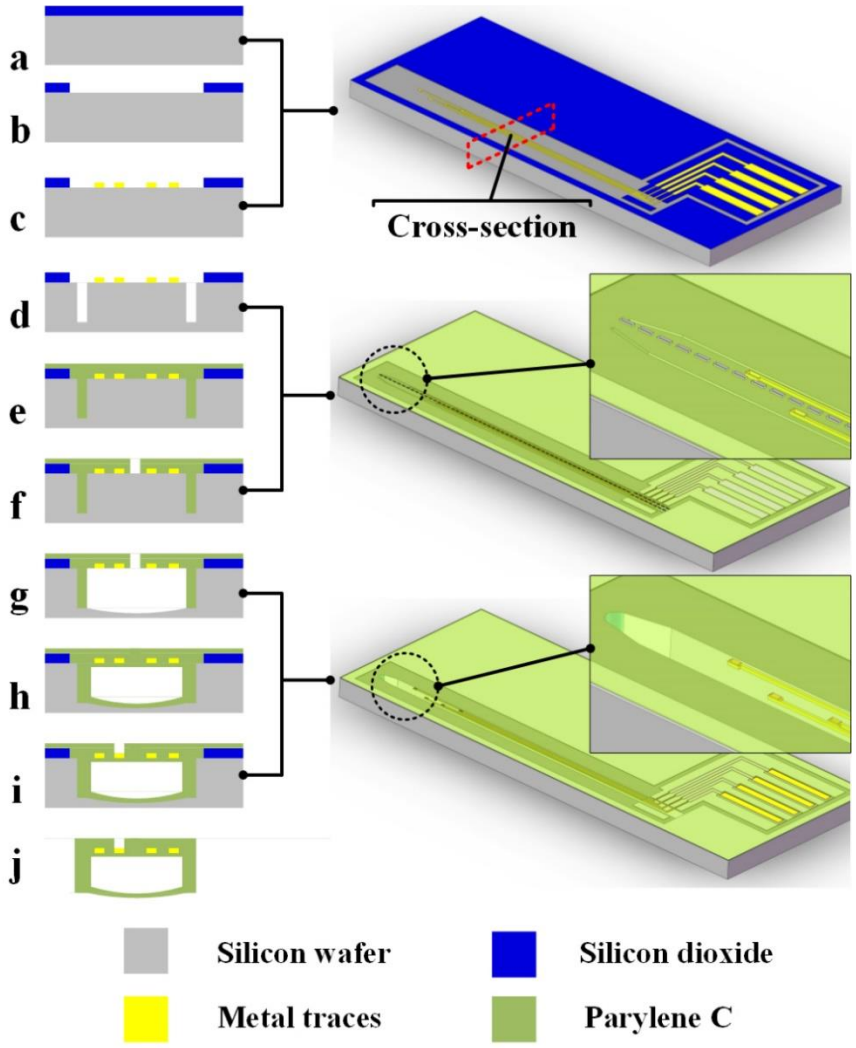

Figure 4-2. The fabrication process of the flexible deep brain neural probe. (a) SiO_2 growth. (b) SiO_2 patterning. (c) Metal evaporation and patterning. (d) Deep RIE to form trenches. (e) Parylene C deposition to fill trenches. (f) Opening parylene windows. (g) XeF_2 silicon isotropic etching. (h) Parylene C deposition to seal the tubular structure. (i) Exposure of electrodes and contact pads. (j) Deep RIE to release the device from the wafer.

The assembly of the device includes the tube insert and making electrical contact to the interface chip at the base of the device. The insertion of the metal wire to the parylene tube was performed under a stereomicroscope. A funnel structure is implemented at the tube inlet to facilitate the insertion of the metal wire. Since parylene is transparent, the progression of the metal wire can be clearly observed. In addition, the diameter of the stainless steel wire was made to be slightly smaller than that of the parylene tube. Consequently, the insertion and removal of the stainless steel wire do not cause any damage to the parylene tube.

A horizontal 4-pin FFC (flexible flat cable) connector (Hirose Electric. Part#: FH19C-4S-0.5SH) was clamped to the bonding pads on the silicon island, making electrical contact with the 4 gold traces. The connector subsequently was encapsulated by marine epoxy to prevent potential short circuits due to the seeping of water or moisture condensation.

Insertion Force characterization

Mechanical insertion tests were performed using 0.6% agarose gel as a neural tissue phantom. The test setup is shown in Fig. 4-3. Agarose gel was attached directly to a Transducer Techniques GSO series load cell (GS0-10) with a resolution of 0.021 mN so that the force of insertion could be monitored during the course of insertion. The force gauge was attached to a caliper stage so that its relative position to the neural probe can be easily adjusted. The movement of the neural probe toward the agarose gel was generated using a syringe pump (MODEL NO. BS-8000). The insertion speed was set to 0.34 mm s^{-1}.

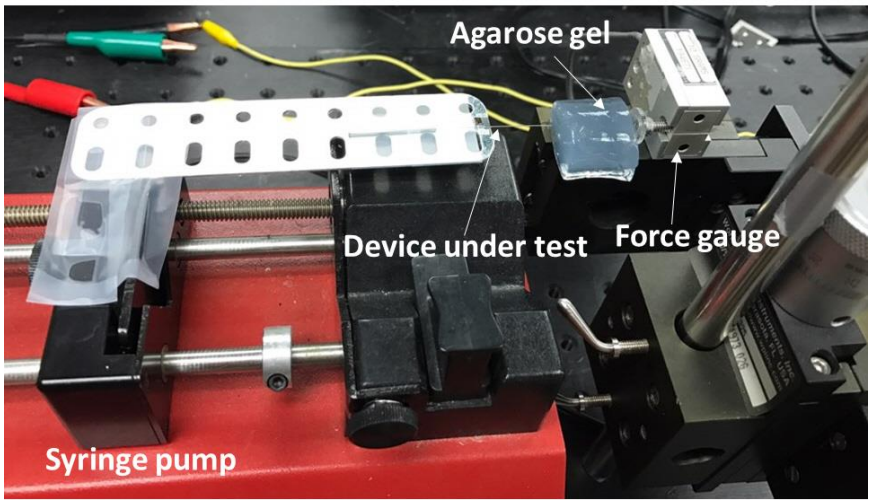

Figure 4-3. Testing setup for the characterization of insertion force.

In vivo animal test protocol

Aseptic surgery was conducted to implant the ultra-long probe into the right amygdala of an adult male Sprague-Dawley rat (100–120 d of age). Among the brain structures of rats, the amygdala was chosen because it is the deepest if implanted dorsoventrally. Briefly, anesthesia was induced and maintained by inhalation of a mixture of isoflurane (2-3% v/v) and air (0.4 l min^{-1}). A stereotaxic frame was used to identify the position of the amygdala. A craniotomy was performed to provide access to the right amygdala. Specifically, a small hole was drilled on the skull above the right basal/central nuclei of the AMG (From bregma, the posterior -1.2 mm, DV -4.5 mm, ML 3.0 mm). Prior to implantation, the tip of the electrode was dipped in 3% 1,1′-dioctadecyl-3,3,3′,3′-tetramethylindocarbocyanine perchlorate (DiI) solution to label the tracks of insertion [112]. Electrophysiological recording from the amygdala was conducted using a Tucker-Davis Technologies Z-series electrophysiological data acquisition system. Neural signals were preamplified and bandpass filtered (300–3000 Hz), and the threshold was set at 2 times the root mean square level. The sampling rate was 25 kHz. The rat's body temperature

was maintained at 37 °C during the implantation. All surgical and non-surgical procedures were in accordance with the guidelines by the IACUC at Wayne State University.

Result

Microfabrication

The results of the fabrication and assembly are shown in Fig. 4-4. In Fig. 4-4 (a) and (b), the device can be seen prior and after the insertion of a stainless-steel wire. The hollow parylene shank is 18.2 mm long, a significant length compared to many other MEMS probes, and very easy to deflect with minimal force, a property desirable to improve chronic stability. The electrodes are 22 μm wide and 73 μm long. The minimum width of the metal traces is 16 μm. The reinforcing wire is a stainless steel needle with a diameter of approximately 130 μm. In the inset of Fig. 4-4 (b), electrodes, stainless steel needle insert, and the transparent parylene tube can be clearly observed. It is worth noting that the inserted metal wire, which does not need to have a sharp tip, is stopped by the tapered sidewalls of the parylene tube. Fig. 4-5 shows a packaged device with an inserted stainless steel needle (130 μm diameter) a 4-pin FFC connector (Hirose Electric. Part#: FH19C-4S-0.5SH) encapsulated by the marine epoxy.

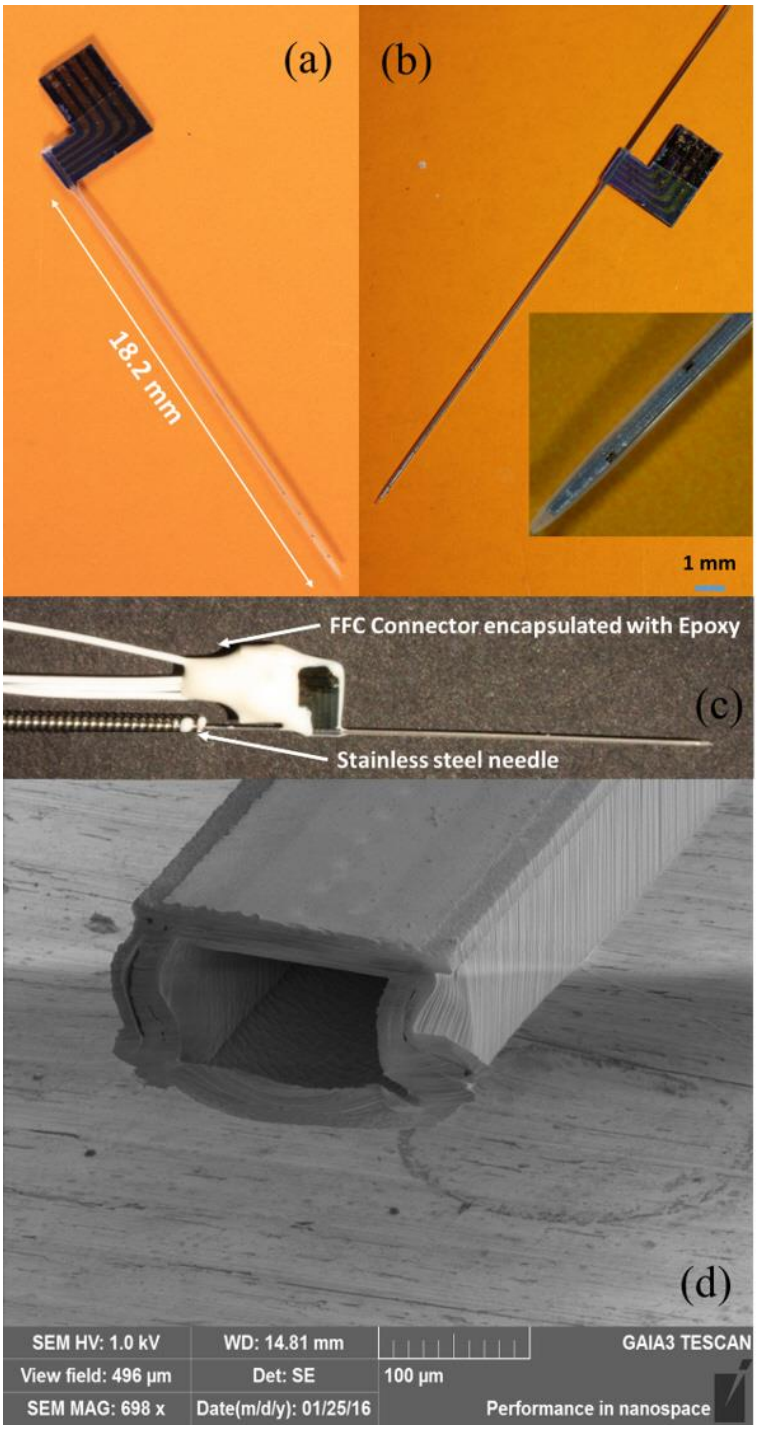

Figure 4-4. (a) Image of the super long probe after fabrication. (b) Image of the super long probe reinforced by a 130 µm diameter stainless steel needle. The inset shows the magnified view of the tip area. Scale bar: 200 µm.

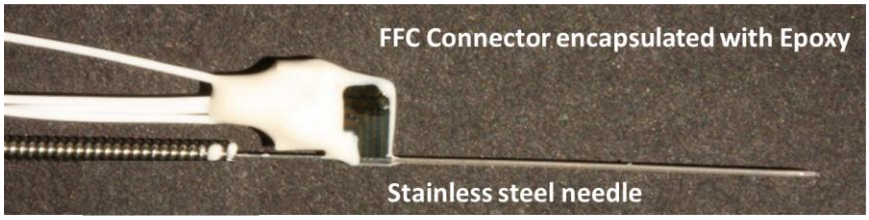

Figure 4-5. Image of the packaged device. An FFC connector was encapsulated with marine epoxy to avoid potential short circuits.

Fig. 4-6 shows a scanning electron microscope (SEM) image of an ultra-long probe shank cut in cross-section to reveal the hollow interior. As discussed in the process flow, the vertical parylene side walls are formed by refilling deep silicon trenches etched by DRIE. Marks of resealed etch windows can be observed on the top surface. Note that the deformation of the cross-section was caused during cutting of the shank by a razor blade.

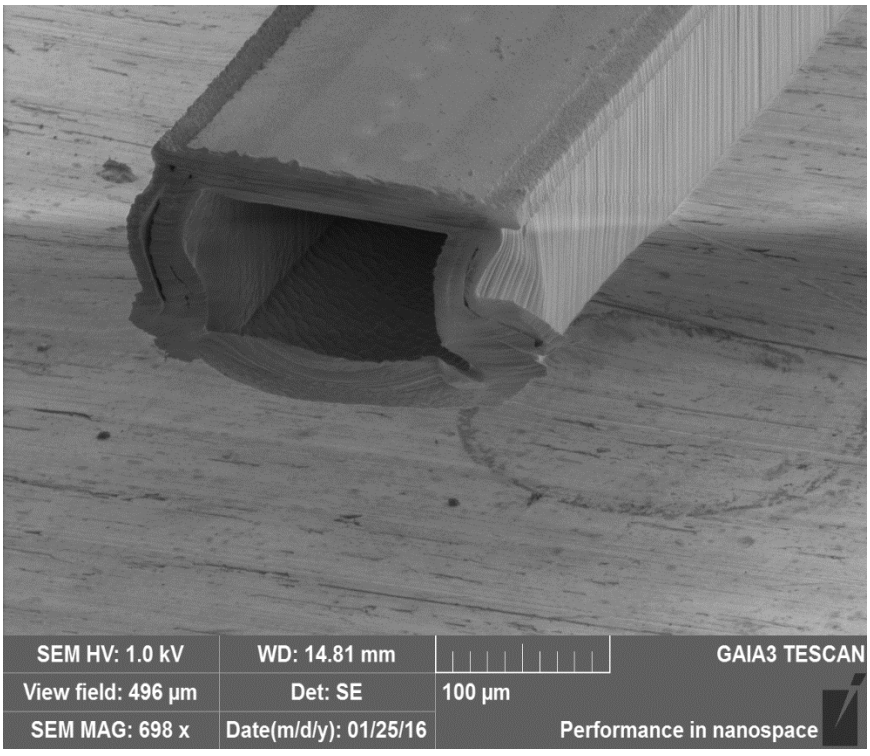

Figure 4-6. SEM image showing the shank of the probe cut in cross-section.

Insertion force Characterization

We repeated the insertion force tests multiple times, and the results showed good reproducibility. The testing results are summarized in Fig. 4-7. Dashed lines represent individual tests. The solid line is the average of the load cell readouts of the insertion force. It seems that the probe needs to penetrate a barrier on the surface with a much larger force. The maximum force during this initial barrier region has an average value of 11.6 mN and a standard deviation of 1.3 mN. This number matches very well with the 11 mN penetration force through rat dura mater of sharpened silicon probes reported by Fekete et al [113]. Goncalves et al reported that the maximum insertion force of 180 μm wide silicon shank in 0.5% agarose gel is 2.65 mN and 12.5 mN in the porcine brain [114]. After passing this barrier, the insertion force dropped abruptly to 1.4 mN and then slowly increased to 2.0 mN when it stopped at a penetration depth of 11 mm. This value is comparable to the reported 1.15 ± 0.51 mN force of a 150 μm diameter tungsten electrode for rat pia mater [115].

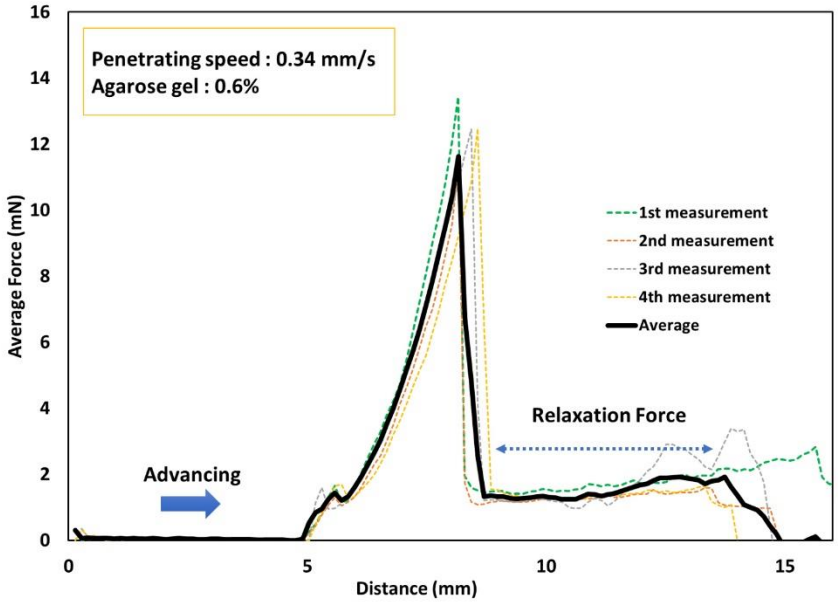

Figure 4-7. The calibrated plot of average axial force encountered by the long probe versus distance as it advanced into 0.6% agarose gel with a speed of 0.34 mm s^{-1}. The average penetration depth is 11 mm.

Impedance characterization

Based on finite element simulation, the bending radius of the shank needs to be less than 1.5 mm to possibly break the gold traces. In the agarose gel test, no buckling or significant deflection of the probe was observed during the course of the insertion due to the inserted metal wire. Therefore, the ultra-long probe will not be damaged during implantation. To confirm this, the impedance of each electrode was measured before and after multiple insertion tests. As shown in Fig. 4-8, the impedance of all electrodes remain almost unchanged, proving that metal traces and probe are well protected by inserted metal wire from a large deflection.

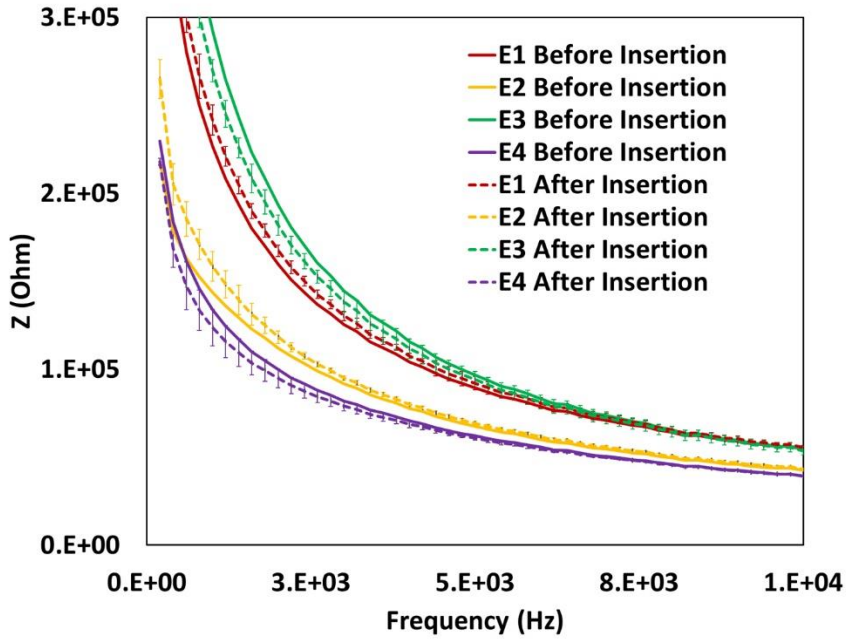

Figure 4-8. Electrode impedances of four sites before and after the agarose insertion test.

Modeling for buckling properties characterization result

The buckling force of the parylene tube shank enhanced by a 130 μm diameter stainless steel wire is estimated using a mechanical model shown in Fig. 4-9. The critical buckling force for a slender beam based on Euler–Bernoulli beam theory is shown below:

$$F_c = \frac{\pi^2 (E_1 I_1 + E_2 I_2)}{(KL)^2}$$

where K is effective column factor, and L is the length of the beam. E_1, E_2, I_1, and I_2 are Young's moduli and area moments of inertia of parylene tube and stainless steel wire, respectively. In our calculation, Young's modulus of parylene C is chosen to be 2.8 GPa [116] and that of stainless steel is 193 GPa [117]. The beam length L is 18.2 mm. It is worth noting that E_1I_1 is only approximately 3% of E_2I_2. Therefore, the buckling force is dominated by the stainless steel wire. By assuming one end of the beam is fixed and the

other end is pinned, the effective column factor K is 0.699. Based on these values, the estimated buckling force of the 18.2 mm long shank is about 160 mN. Sharp et al used a flat-tipped 100 µm diameter stainless-steel probe to penetrate through all sub-cranial connective tissue, including dura, into cerebrum of mouse brains and reported an average penetration force of 10.9 mN [118]. Therefore, our super-long probes, enhanced by stainless steel needles, should be able to penetrate the dura layer. Fekete et al reported insertion forces of 11 mN for sharpened and 49 mN for unsharpened silicon probes in rats [113]. Based on these two buckling forces, the estimated maximum achievable length of our probe enhanced by 130 µm stainless steel wire would be 67 mm and 31 mm respectively.

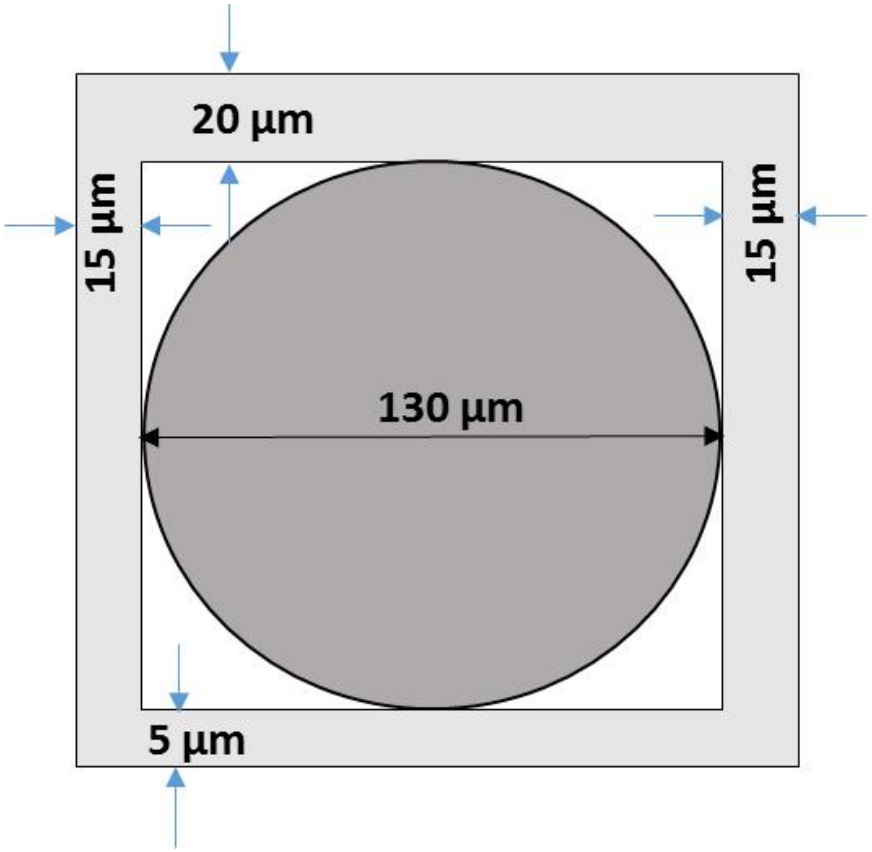

Figure 4-9. A mechanical model for buckling force calculation.

It is worth noting that after implantation, the stainless steel wire can be easily removed since the lateral dimension of the parylene tube is slightly larger than the diameter of the metal wire. The left-behind flexible parylene tube probe is able to reduce the stress caused by micromotions [119]. Furthermore, an optical fiber can be inserted, delivering light to deep brain structures for optogenetic modulation. For example, in Fig. 4-10 (a) the probe tip where green laser light emitted from an optical fiber can be clearly observed. Fig. 4-10 (b) illustrates the light emitted from the tip of the probe inserted in 0.6% agarose gel. In this demonstration, a 125 μm diameter, 50 μm core multimodal optic fiber (Thorlabs, FG050LGA. 0.22 NA) was used and connected to a green diode-pumped solid-state (DPSS) laser (SLOC, GL532T3-100FC, 532 nm) via an FC/PC connector. The cone shape emitted light from the end of the fiber has an angle of about 60°.

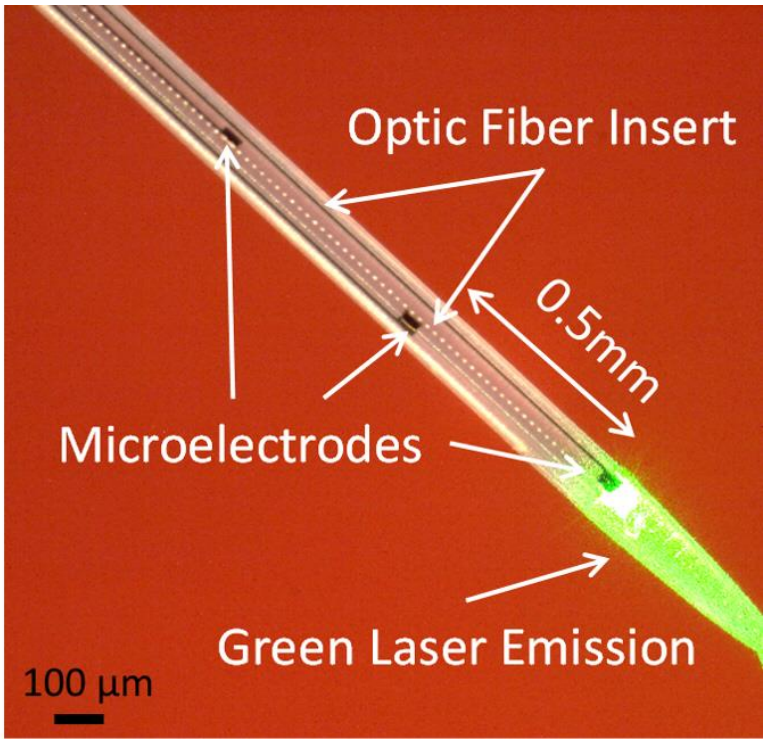

(a)

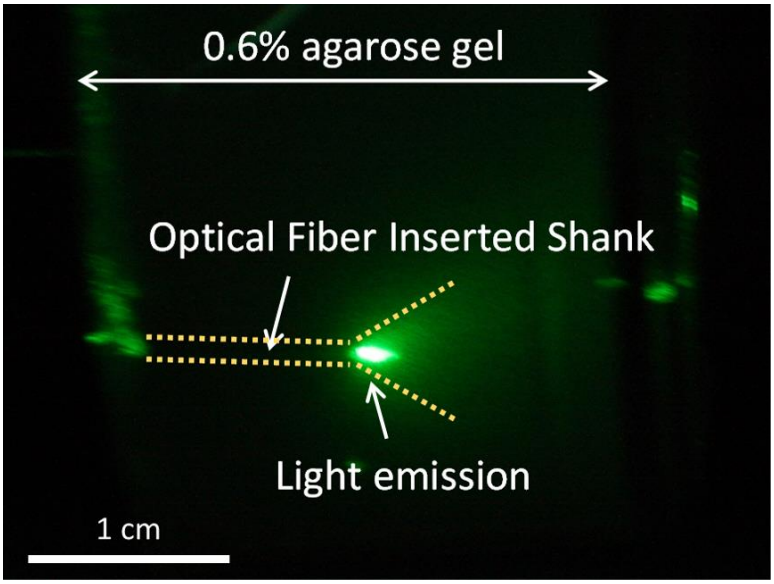

(b)

Figure 4-10. (a) Micrograph of the probe tip where green laser light emitted from an optical fiber can be clearly seen through the transparent parylene sheath (b) image of the light-emitting from the tip of the probe inserted into 0.6% agarose gel. The shank and emitted cone shape light were delineated by dashed lines.

An image of the rat with an acutely implanted ultra-long probe is shown in Fig. 4-11 (a). Local field potential (LFP) has been successfully recorded as shown in Fig. 4-11 (b) [77]. One channel (the third electrode) had a high noise level. After implantation, the impedance of this electrode was found to be 132 kΩ at 1 kHz, about 3-4 times of the other three electrodes. This was probably caused by an accidental large bending of the probe during handling. Further studies may help characterize the recording abilities of this probe; however, the preliminary data suggests the probe serves the function we set out to achieve.

(a)

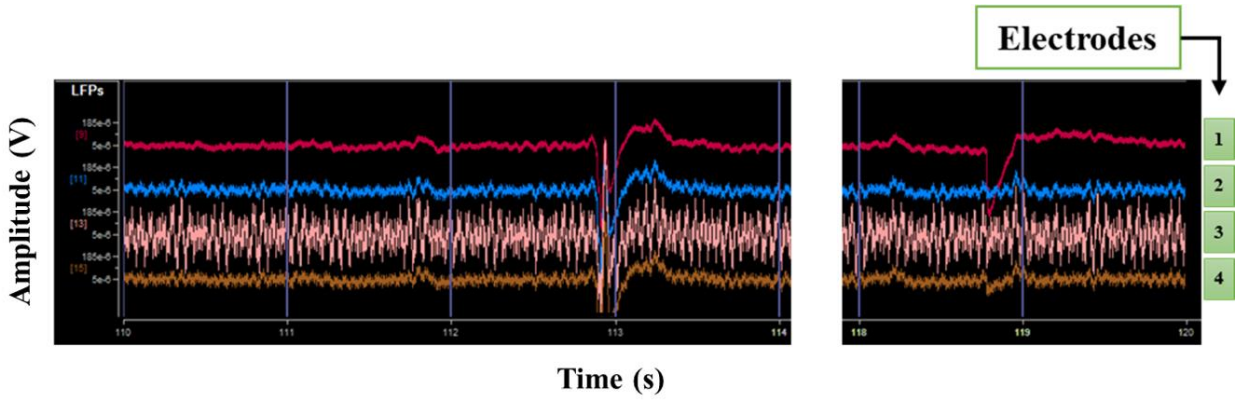

(b)

Figure 4-11. (a) Photograph showing surgical implantation of the ultra-long probe and electrophysiological recording setup. Note that the second hole in the back of the rat's head was drilled in order to release intracranial pressure to avoid a brain hernia during experimentation. (b) LFP data recorded from the amygdala.

Discussion

The main purpose of this paper is to introduce a new technology of developing ultra-long neural probes that can target deep brain structures or brains of large animals. To prove the concept, we only developed single-shank devices. Using an identical

fabrication process, we can readily fabricate multi-shank devices, and also devices with multiple silicon islands which can be folded to make 3D arrays of the electrode [120, 121]. The current 18.2 mm long shank enhanced by 130 μm stainless steel wire has a buckling force of ~160 mN. Based on the 11 mN maximum penetration force [113], the probe length can be extended to 67 mm. The diameter of the inserted metal wire can be increased to further increase the length.

The microfabrication of parylene tube is based on DRIE, parylene conformal coating and XeF_2 isotropic silicon etching, which is a robust and well-established process. Other groups reported similar methods based on isotropic silicon etching and sealing with polysilicon or SiO_2 to integrate microchannels with silicon neural probes [110, 111]. In our method, the silicon is completely removed, resulting in flexible parylene tube probes. The structure is actually asymmetric with the top parylene layer thicker than the bottom layer. However, this asymmetric mechanical structure will not be an issue during implantation since the rigidity is dominated by the inserted metal wire. To avoid damage to the parylene tube during the process of inserting and removing the stainless steel wire, the diameter of the stainless steel wire was sanded to be slightly smaller than that of the parylene tube.

More comprehensive animal tests will be carried out in the future. For instance, chronic *in vivo* tests to compare the tissue responses of parylene tubes with and without metal wires will be of great interest. The parylene tube can also function as a microfluidic channel for chemical delivery. Such a capability is highly desirable for probing neural circuits as demonstrated by others [94, 95]. Thanks to the transparency of parylene, an optical fiber can be inserted (Fig. 4-8), enabling the delivery of light to deep brain

structures for optogenetic modulation. A unique feature of our device is that the inserted optical fiber can move along the depth of the parylene tube, modulating neurons at different layers. A multi-lumen structure, readily fabricated by adding additional parylene side walls, can be implemented to enable both optogenetic modulation and chemical delivery. Therefore, ultra-long neural probes developed by this technology can be integrated with multi-modal modulation capabilities without complicating the fabrication process at all.

Conclusion

Ultra-long probes based on a parylene tube structure have been successfully demonstrated. Single-shank prototypes with a shank length of 18.2 mm have been microfabricated based on a process consisting of parylene filling of deep silicon trenches, XeF_2 isotropic silicon etching and parylene resealing. The flexible parylene tube shank can be mechanically strengthened by inserting a metal wire. The insertion force with a 130 μm stainless steel reinforcing wire has been characterized in an agarose brain phantom. A prototype has been implanted into the amygdala of a rat and recorded neural signals. By taking advantage of the parylene tube, more advanced ultra-long probes integrated with electrical, chemical and optogenetic modulation capabilities can be readily developed to interrogate neural circuits of deep brain structures or brains of large animals.

Chapter 5 Braided electronics and sensors based on parylene smart tubes[3]

Introduction

Wearable electronics and sensors have received a lot of attention recently due to their potential impact on healthcare, entertainment, and military applications. Among various methods of developing wearable devices, one approach of special interest is based on functional fibers, yarns, or tubes. For instance, conventional cotton threads have been transformed into smart yarns using a polyelectrolyte-based coating with carbon nanotubes [122]. Mostafalu et al. reported pH sensors and microfluidics-based on cotton yarns [123]. Tang et al. developed highly stretchable silicone protected core-sheath piezoresistive fibers using a wet-spinning method [124]. Piezoelectric fiber nanogenerators have been developed by cylindrically covering carbon fibers with textured zinc oxide (ZnO) thin films [125].

Braiding and weaving techniques have been employed to enhance the functionality and mechanical strength of smart fibers or smart yarns. For instance, conductive fibers were developed by twisting or spinning carbon nanotubes [126, 127] and served as artificial muscles [128]. Do and Visell reported flexible and stretchable sensors formed by twisting two silicone microtubes filled with liquid metal [58]. Huang et al. reported yarn-based piezoresistive sensors by wrapping the carbon-coated fibers with regular polyester fibers [3]. Electrospinning is also a common method to develop smart fibers, such as the nanofiber-structured single yarn sensor reported by Wu et al. [5].

In this work, we report the development of a new type of braided sensors and electronics based on parylene tubes. The unique advantage is its post-CMOS and post-MEMS compatibility, which enables the integration of high-performance circuits and sensors [73, 108]. In this work, metal piezoresistors are integrated for proof-of-concept purpose. The tubular structure also allows the further tuning of mechanical properties and the incorporation of more functionalities.

Design and fabrication

Design

The device design is schematically shown in Fig. 5-1. The three hollow parylene tubes, which will be braided together, are integrated with metal piezoresistors. Tube structure is considered to be more robust than ribbon and enables the incorporation of multiple functions such as chemical and drug delivery. The contact pads of piezoresistors are formed on the silicon pedestal. The silicon pedestal is also connected with three injection legs with channel inlets, which enable the filling of the parylene tubes with strengthening materials such as polydimethylsiloxane (PDMS).

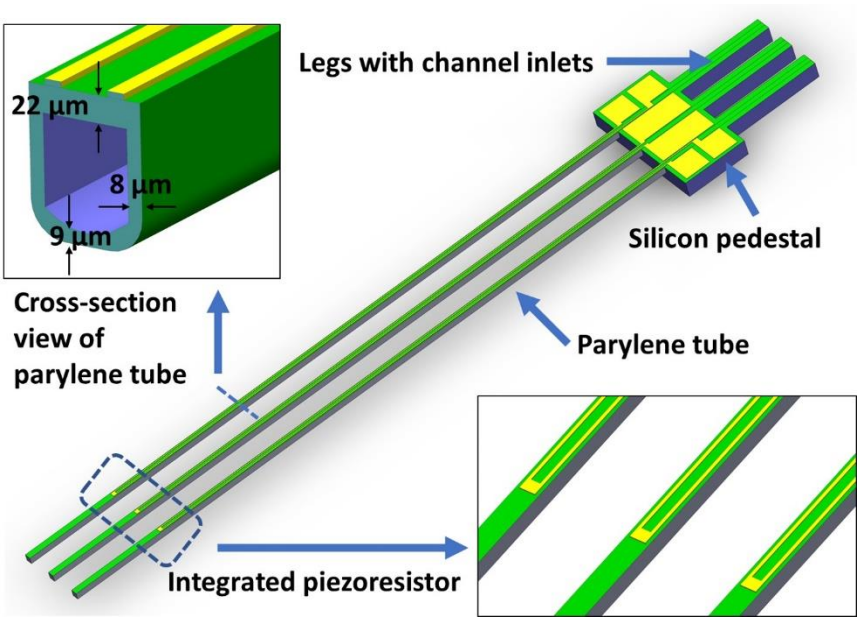

Figure 5-1. A 3-D schematic of device design with a parylene tube cross-sectional view and a magnified view of integrated piezoresistors.

The device was microfabricated based on a well-established process we have reported in the past work [129]. Fig. 5-2 shows a cross-sectional view of each step of the fabrication flow. First, deep reactive ion etching or DRIE (Plasmatherm SLR-770) was performed on a silicon wafer to form 8 µm wide and 100 µm deep trenches. Subsequently, these trenches were refilled with 10 µm parylene-C (PDS2010, Specialty Coating System), serving as the sidewalls of parylene tubes. Next, columns of discrete holes with a dimension of 8 µm × 20 µm and a pitch of 40 µm were opened using oxygen plasma (DryTek, DRIE 184) in the parylene-C layer between trenches formed in the first step. Then through these openings, XeF_2 etching was performed to etch the silicon underneath. Since XeF_2 silicon etching is isotropic, the discrete parylene holes would lead to a continuous channel in the silicon substrate. The channel depth was controlled to be around 125 µm, and the width was limited by previously formed parylene sidewalls, which

were 100 μm apart. Then, another 9 μm parylene-C was deposited to form an enclosed parylene tube by coating inside of the channel and seal the etching holes simultaneously, by taking advantage of the conformal nature of parylene deposition. Next, a combination of the Ti/Au/Ti layer was e-beam evaporated to a thickness of 20/200/20 nm and patterned to form piezoresistors and contact pads. Then, the third layer of parylene was deposited to isolate metal traces. Next, contact pads were opened, and the outer lines of the device were delineated using oxygen plasma. Lastly, frontside and backside DRIE were performed to release the devices.

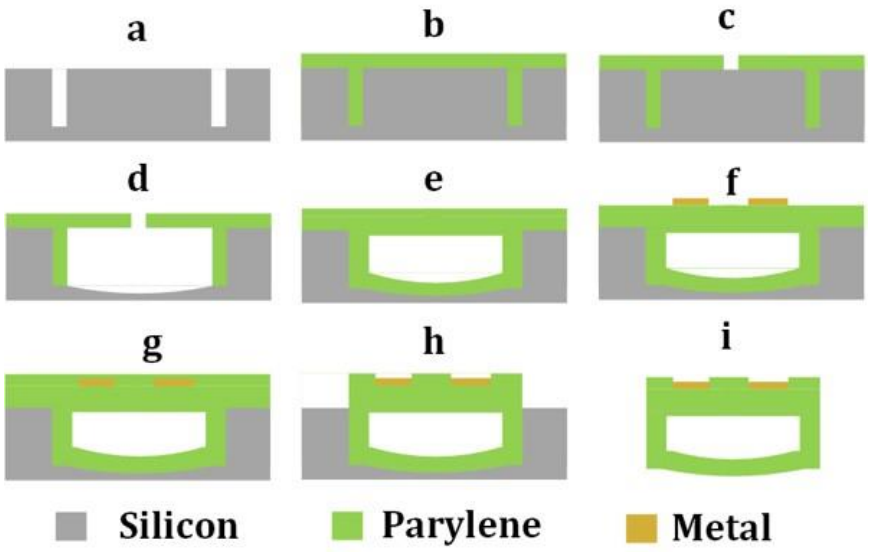

Figure 5-2. Cross-section view of the simplified fabrication flow. a. DRIE to form vertical trenches; b. Parylene deposition to refill the trenches; c. Oxygen plasma RIE to open discontinuous holes; d. XeF_2 isotropic silicon etching to form a continuous channel; e. Parylene deposition to form a sealed channel; f. Ti/Au/Ti E-beam evaporation; g. Parylene deposition to insulate metal layer; h. Oxygen plasma RIE to expose contact pads and delineate device outer line; i. Release the parylene tube by front and backside DRIE.

Braiding and assembly

Among many triple-strand braiding methods, we have chosen the most traditional method for its simplicity. To facilitate the braiding process, each parylene tube was glued with a polymer extension wire with a similar diameter. As shown in Fig. 5-3, to start braiding, the left and right extension wires were attached to a rotary bar with an opening angle around 15 º while the middle wire remained freestanding. Then after the middle wire was moved up slightly (step 1), the rotary bar was rotated by 180 º to twist left and right wires (step 2). Next, the middle wire was moved down (step 3) and subsequently the rotary bar was rotated by another 180 º to cross the left and right wires over the middle one (step 4). This braiding loop then repeated, and the pitch length between each twist is mainly determined by the initial open-angle of the left and right wires. Finally, marine epoxy was used to glue the ends of three tubes.

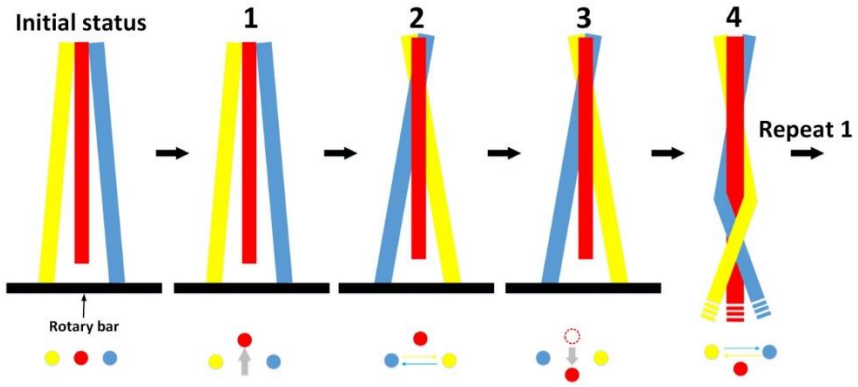

Figure 5-3. A simplified illustration of braiding method: 1. move the middle wire up; 2. rotate the rotary bar by 180 º to form a cross between left and right tubes; 3. move the middle wire down over the cross; 4. rotate the bar by another 180 º to form the second cross above the middle tube.

Fabricated and assembled devices

A fabricated device with three parylene tubes is shown in Fig. 5-4 (a). In this work, both triple-shank and single-shank devices were fabricated with identical dimensions of

parylene tubes. The total length and width of each parylene tube are 21.3 mm and 100 μm respectively. In addition, polyimide tubes can be connected to the legs of the silicon pedestal to inject PDMS or other aiding materials into parylene tubes. Fig. 5-4 (b) shows the SEM (Scanning Electron Microscopy) image of three braided parylene tubes. The piezoresistor was designed as a U-shape metal trace which is partially shown in Fig. 5-4 (c). The resistances were in a range of 400 to 600 Ω.

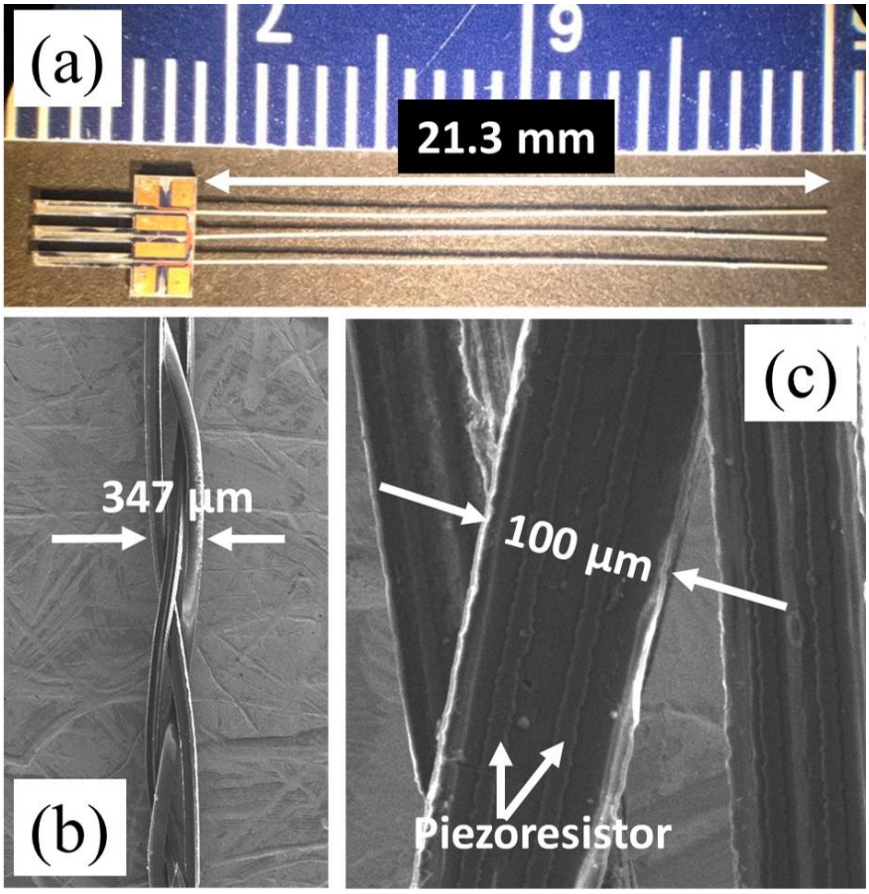

Figure 5-4. (a) Fabricated three-shank device; (b) SEM image of a braided device based on three parylene tubes; (c) magnified SEM image of parylene tubes.

Characterization

Deflection and Stretching force

We first characterized the stretching force for three different devices: empty single parylene tube, PDMS-filled single parylene tube, and three-shank braided device. The testing setup consists of a 150-gram TRANSDUCER TECHNIQUES load cell and a NEWPORT linear moving stage & piezo motion controller set, as shown in Fig. 5-5. The load cell excitation voltage was 10 V and the speed of the moving stage was set to 0.4 mm/s. The voltage output of the load cell was amplified and measured with a sampling rate of 10 Hz using a National Instrument data acquisition board (NI-DAQmx).

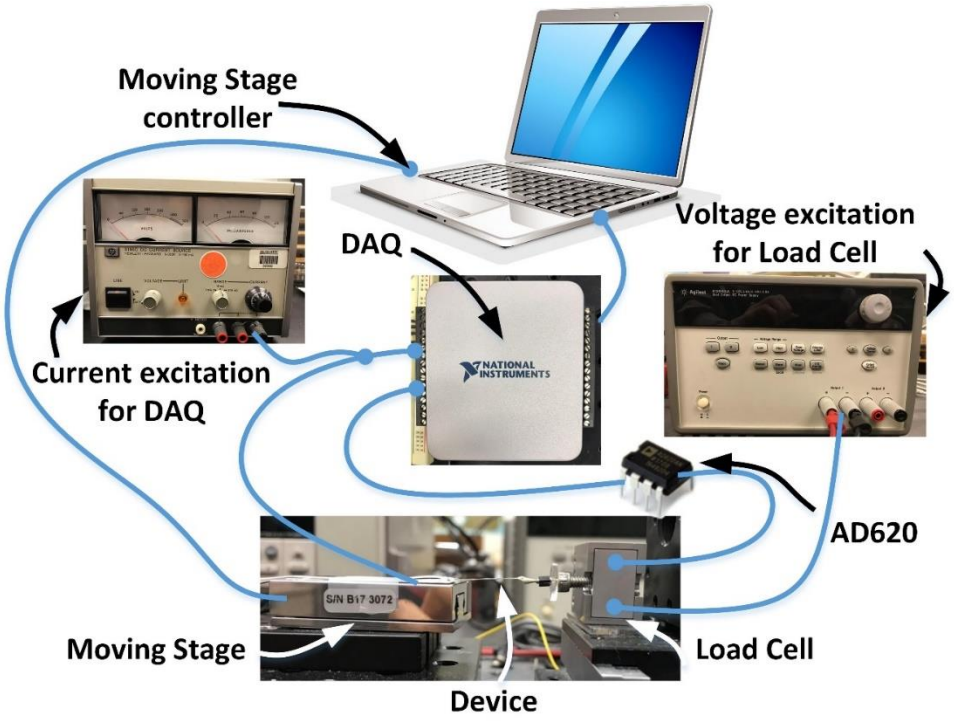

Figure 5-5. Measurement setup for mechanical property and strain gauge sensitivity characterization.

Fig. 5-6 shows the deflection force as a function of displacement with a sampling rate of 10 Hz between a single-shank device and a single-shank device filled with PDMS

(10:1) in the parylene tube. The force was applied at the same position of each shank, and the output voltage was calibrated, and converted into force. The measurement was conducted for the purpose of investigating the maximum curvature force, and it started from an initial force of 1.1 mN which was generated by the fixture of the sensor. From the figure, the deflection force for the single-shank with PDMS was 0.45 mN, larger than the single-shank which is 0.1 mN due to the mechanical support of PDMS. From Fig. 5-7, it can be observed that PDMS makes little contribution to the tensile strength of the parylene tube due to the much higher Young's module of parylene-C (2.8 GPa) [116]. On the other hand, the injected PDMS can enhance the transverse bending strength and avoid kinks of parylene tubes [73]. Both single parylene tube devices fractured when the strains reached 2 %. In comparison, the braided device fractured at the strain of 3.4 % and a larger stretching force was observed.

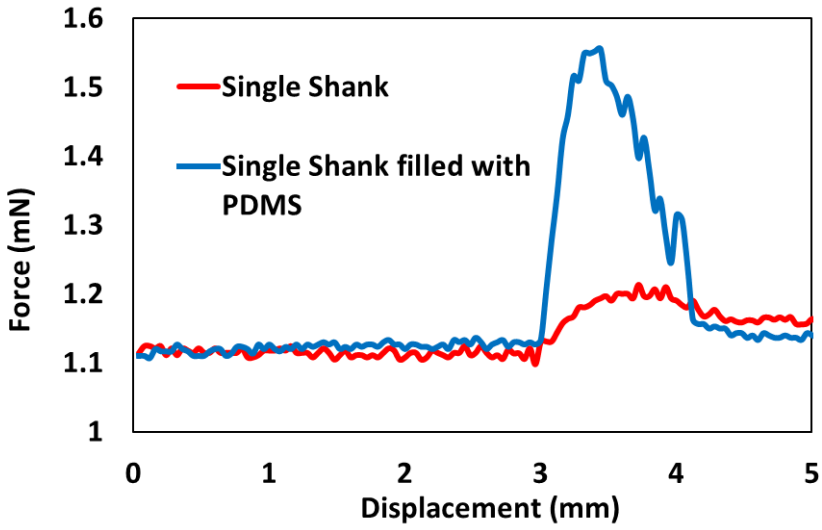

Figure 5-6. Comparison of deflection force between single and single shank filled with PDMS as a function of displacement.

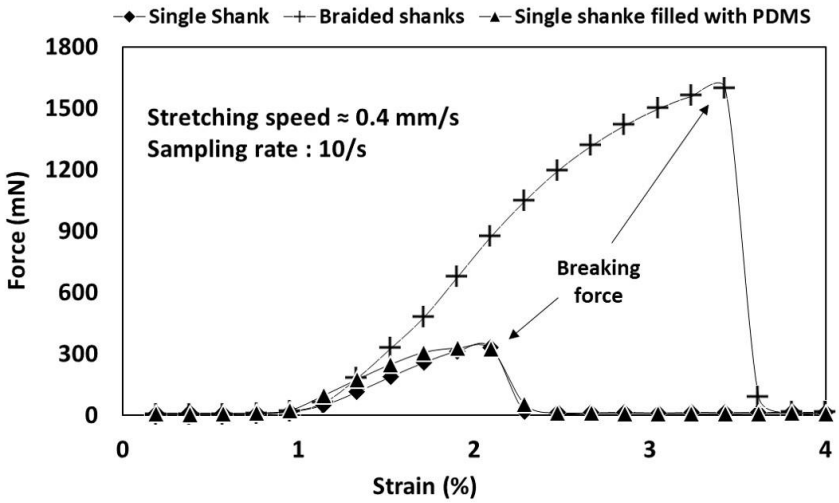

Figure 5-7. Comparison of stretching forces of the single parylene tube, single parylene tubes filled with PDMS, and braided device.

Strain gauge

In order to demonstrate the capability of our device to work as a strain gauge, we monitored the strain and piezoresistor simultaneously. As shown in Fig. 5-8, the gauge factor of the piezoresistor on a single parylene tube was around 1.04. The device under test fractured at a force of 267 mN and the total resistance change during this period is around 26 Ω.

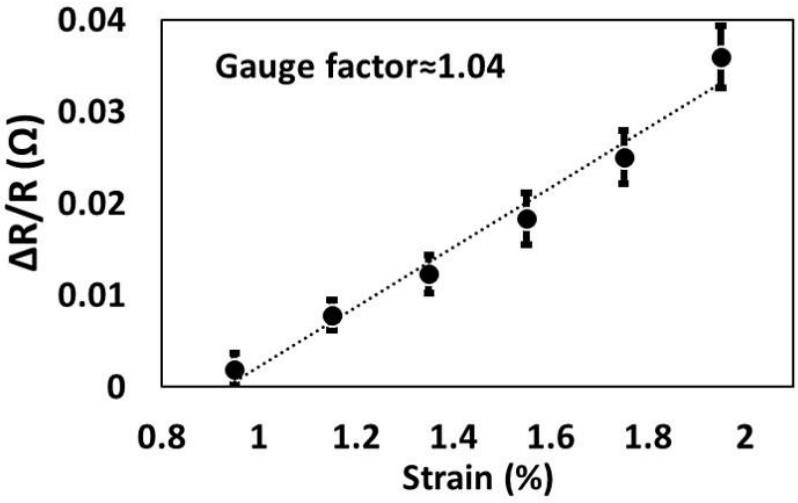

Figure 5-8. Average resistance changes as a function of the strains of a single tube device.

The strain sensitivity of braided devices was characterized by applying cyclic strains as shown in Fig. 5-9 (a). Baseline shifts are observed in the latter half of 0.95% strain test and 1.42% strain test since the initial status was difficult to control for a yarn or string type device. In addition, the movement among the parylene tubes could lead to baseline drift. Such an issue can be avoided by coating another layer of parylene to prevent braided tubes from moving. The average resistance change as a function of the mechanical strain is plotted in Fig. 5-9 (b). The average gauge factor is about 1.05 which is consistent with reported values in literature [130, 131].

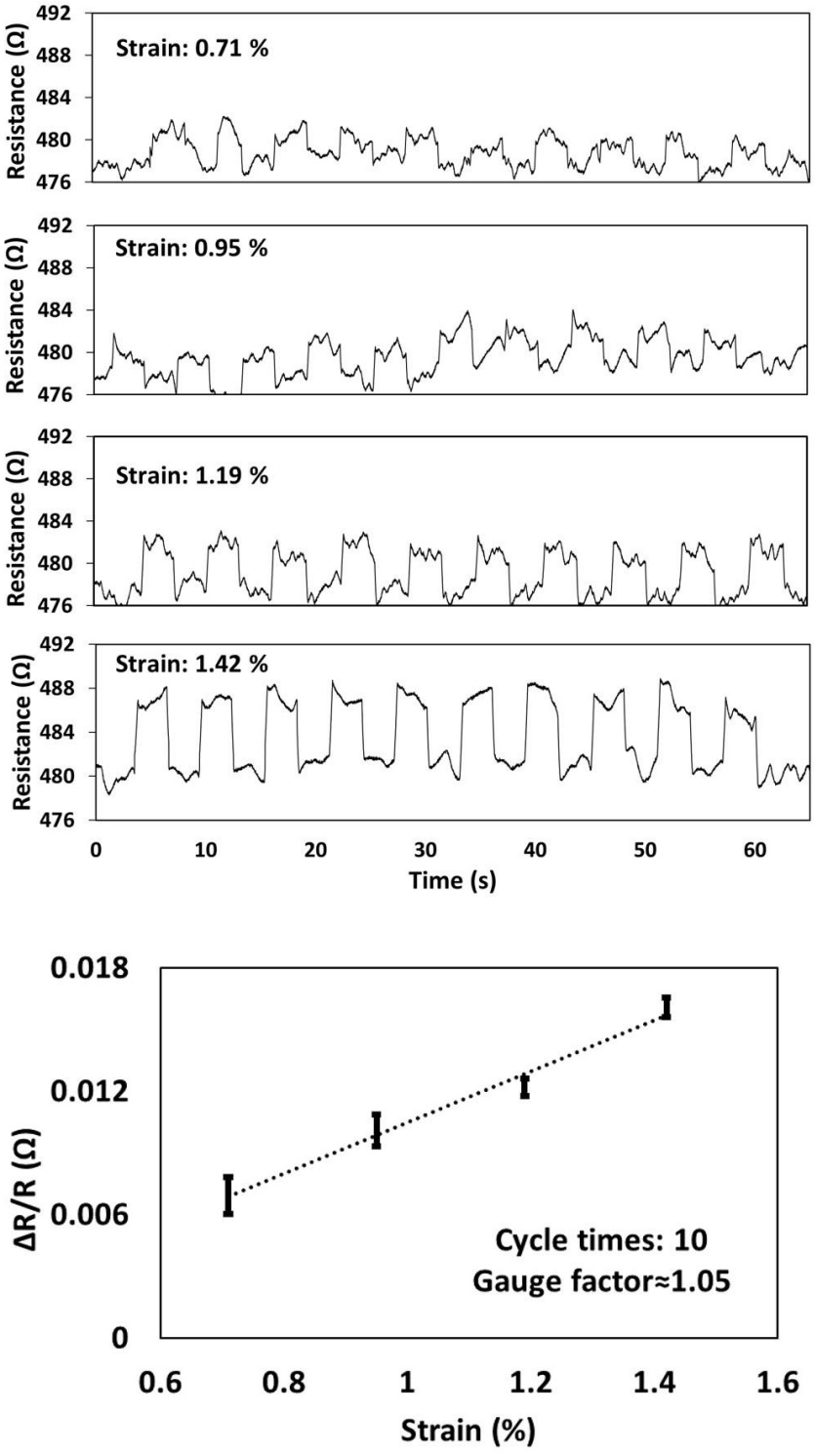

Figure 5-9. (a) Piezo-resistive sensitivities for the braided device under cyclic strains. (b) Average resistance changes as a function of mechanical strain.

Applications

For a real application, preliminary respiratory monitoring has been demonstrated for the proof-of-concept purpose. The braided device was simply attached directly to the chest of a healthy male subject by using isolation tape. The person under test kept his usual breathing pace. The measurement lasted for half a minute with a sampling rate of 100/s. As shown in Fig. 5-10, the respiration was successfully detected by the braided device. The resistance change was between 5 to 10 Ω, depending on the depth of the breath. Based on the resistance change, the maximum strain experienced by the braided device was 1.2% and the corresponding stress was 1.8×10^7 Pa.

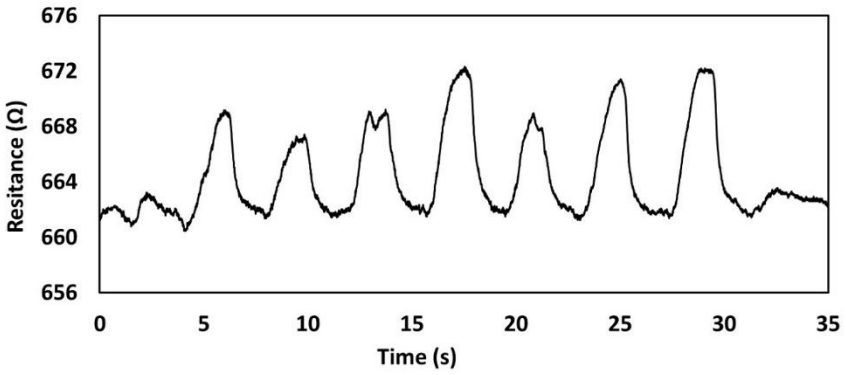

Figure 5-10. Respiration monitoring result by measuring the piezoresistor of a braided device attached to the chest.

Beyond wearable applications, the developed technology can also benefit medical implants. For instance, one potential application of our braided device is a spinal cord neural probe. The spinal cord is probably the most challenging site to implant neural probes due to the large motion of the spinal cord [57]. The mechanical flexibility and strength of our technology make it an excellent candidate for developing spinal cord interfaces. Compared to the device reported in [57], the new technology reported here allows the integration of multiple electrodes or other active devices along the length

direction. Moreover, the tubular structure enables in-situ chemical delivery or other functions such as pneumatic actuation and optogenetic modulation [22]. The reliability of the braided device will be improved by implementing serpentine metal traces and smaller braiding pitches.

Conclusion

In summary, we have demonstrated a method for making yarn-like stretchable electronics and sensors by braiding parylene tubes. In this work, metal piezoresistors were integrated into the parylene tubes for the purpose of proof-of-concept. The devices have been braided using a traditional three-strand method. Stretching tests show that the yield strain and strength of braided devices are larger than those of single parylene tubes. In addition, the piezoresistive sensing of the braided device has been characterized and demonstrated for respiration monitoring. It is worth noting that the fabrication process is post-CMOS and post-MEMS compatible, enabling the integration of high-performance circuits and sensors based on high-temperature materials. For instance, silicon MOSFETs (metal-oxide-semiconductor field-effect transistors) [73], silicon pressure sensors and flow sensors [108] have been successfully integrated on parylene tubes previously. This capability, together with the tubular structure, will greatly enhance the functionality of braided devices.

CHAPTER 6 : FUTURE WORK

So far we have introduced a flexible Ag/AgCl micro reference electrode, flexible deep brain neural probes, and probes that are braided to enhance the mechanical properties. The results of the work have shown the tremendous possibilities of integrating even more functions and sensors on a single device. Our future work will not only focus on the further optimization of the device characteristics but also realizing the diverse applications by integrating different sensors and modifying the device structures. Fig. 6-1 shows an example of a concept how we are going to approach the ideas of the integration. Each probe has its unique function which would either work itself or provide certain conditions for other probes. The first one is chemical sensing electrodes that are based on our previously presented reference electrodes. The number of the sensing elements can be flexible based on the target elements in which we are interested. For example, three sensing electrodes can possibly be put into the design, each of them would work as a pH sensing, Oxygen sensing, or other ionic elements sensing electrode by depositing ionic sensitive materials such as IrO_x for pH sensing. The second and the third one can both act as the neural probes with different objectives. Stimulation and recording electrodes can be interchangeably distributed on each probe, and the number could be quite flexible which allows the electrode arrays. Both the second and the third probes have been designed to be hollow that allows simultaneous optic modulation by inserting an optic fiber, and drug delivery by injecting the chemicals through the inlet.

Although each probe may have the slightly different physical structures to each other that make them look challenging to be fabricated through single process flow, they

in effect share very similar and well-established fabrication flow and nothing different compared to the one for making a single probe.

Further investigations of materials for sensing electrodes, optic fibers, and chemicals will be done. If successful, dynamic and comprehensive in-vivo studies will be enabled by simultaneous data collecting and analyzing.

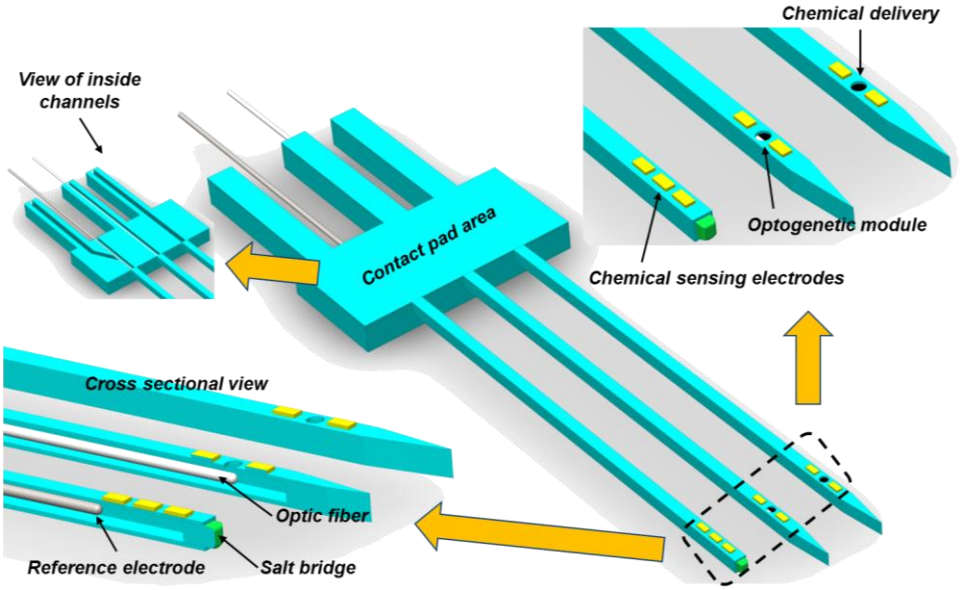

Figure 6-1. A concept of the multifunctional micro probe that is integrated with a chemical sensing probe, a neural probe with optic modulation, and a neural probe with drug delivery function.

REFERENCE

[1] Y. Xu, “Post-CMOS and Post-MEMS Compatible Flexible Skin Technologies: A Review,” *Ieee Sensors Journal,* vol. 13, no. 10, pp. 3962-3975, Oct, 2013.

[2] R. B. Katragadda, and Y. Xu, “A novel intelligent textile technology based on silicon flexible skins,” *Sensors and Actuators a-Physical,* vol. 143, no. 1, pp. 169-174, May 2, 2008.

[3] C. T. Huang, C. L. Shen, C. F. Tang, and S. H. Chang, “A wearable yarn-based piezo-resistive sensor,” *Sensors and Actuators a-Physical,* vol. 141, no. 2, pp. 396-403, Feb 15, 2008.

[4] K. Cherenack, and L. van Pieterson, “Smart textiles: Challenges and opportunities,” *Journal of Applied Physics,* vol. 112, no. 9, Nov 1, 2012.

[5] S. H. Wu, P. H. Liu, Y. Zhang, H. N. Zhang, and X. H. Qin, “Flexible and conductive nanofiber-structured single yarn sensor for smart wearable devices,” *Sensors and Actuators B-Chemical,* vol. 252, pp. 697-705, Nov, 2017.

[6] T. Yan, Z. Wang, Y. Q. Wang, and Z. J. Pan, “Carbon/graphene composite nanofiber yarns for highly sensitive strain sensors,” *Materials & Design,* vol. 143, pp. 214-223, Apr 5, 2018.

[7] Y. L. Wang, J. Hao, Z. Q. Huang, G. Q. Zheng, K. Dai, C. T. Liu, and C. Y. Shen, “Flexible electrically resistive-type strain sensors based on reduced graphene oxide-decorated electrospun polymer fibrous mats for human motion monitoring,” *Carbon,* vol. 126, pp. 360-371, Jan, 2018.

[8] J. H. Kim, G. H. Lee, S. Kim, H. W. Chung, J. H. Lee, S. M. Lee, C. Y. Kang, and S. H. Lee, “Flexible deep brain neural probe for localized stimulation and

detection with metal guide," *Biosens Bioelectron,* vol. 117, pp. 436-443, Jun 20, 2018.

[9] V. Castagnola, E. Descamps, A. Lecestre, L. Dahan, J. Remaud, L. G. Nowak, and C. Bergaud, "Parylene-based flexible neural probes with PEDOT coated surface for brain stimulation and recording," *Biosens Bioelectron,* vol. 67, pp. 450-7, May 15, 2015.

[10] C. Boehler, C. Kleber, N. Martini, Y. Xie, I. Dryg, T. Stieglitz, U. G. Hofmann, and M. Asplund, "Actively controlled release of Dexamethasone from neural microelectrodes in a chronic in vivo study," *Biomaterials,* vol. 129, pp. 176-187, Jun, 2017.

[11] P. J. Rousche, D. S. Pellinen, D. P. Pivin, Jr., J. C. Williams, R. J. Vetter, and D. R. Kipke, "Flexible polyimide-based intracortical electrode arrays with bioactive capability," *IEEE Trans Biomed Eng,* vol. 48, no. 3, pp. 361-71, Mar, 2001.

[12] X. B. Jiao, Y. Wang, and Q. Qing, "Scalable Fabrication Framework of Implantable Ultrathin and Flexible Probes with Biodegradable Sacrificial Layers," *Nano Letters,* vol. 17, no. 12, pp. 7315-7322, Dec, 2017.

[13] !!! INVALID CITATION !!! [13-15].

[14] H. C. Tian, J. Q. Liu, X. Y. Kang, Q. He, B. Yang, X. Chen, and C. S. Yang, "Flexible multi-channel microelectrode with fluidic paths for intramuscular stimulation and recording," *Sensors and Actuators a-Physical,* vol. 228, pp. 28-39, Jun 1, 2015.

[15] C. Li, P. M. Wu, J. Han, and C. H. Ahn, “A flexible polymer tube lab-chip integrated with microsensors for smart microcatheter,” *Biomed Microdevices,* vol. 10, no. 5, pp. 671-9, Oct, 2008.

[16] Y. W. Zhao, K. Wang, S. W. Li, P. Zhang, Y. Shen, Y. Fu, Y. Zhang, J. Zhou, and C. Y. Wang, “Polydimethylsiloxane (PDMS)-Based Flexible Optical Electrodes with Conductive Composite Hydrogels Integrated Probe for Optogenetics,” *Journal of Biomedical Nanotechnology,* vol. 14, no. 6, pp. 1099-1106, Jun, 2018.

[17] M. HajjHassan, V. Chodavarapu, and S. Musallam, “NeuroMEMS: Neural Probe Microtechnologies,” *Sensors,* vol. 8, no. 10, pp. 6704, 2008.

[18] J. P. Seymour, F. Wu, K. D. Wise, and E. Yoon, “State-of-the-art MEMS and microsystem tools for brain research,” *Microsystems &Amp; Nanoengineering,* vol. 3, pp. 16066, 01/02/online, 2017.

[19] !!! INVALID CITATION !!! [21].

[20] G. Buzsáki, E. Stark, A. Berényi, D. Khodagholy, Daryl R. Kipke, E. Yoon, and K. D. Wise, “Tools for Probing Local Circuits: High-Density Silicon Probes Combined with Optogenetics,” *Neuron,* vol. 86, no. 1, pp. 92-105, 2015 Apr 08, 2015.

[21] A. Weltman, J. Yoo, and E. Meng, “Flexible, Penetrating Brain Probes Enabled by Advances in Polymer Microfabrication,” *Micromachines,* vol. 7, no. 10, pp. 180, 2016.

[22] E. G. R. Kim, H. E. Tu, H. Luo, B. Liu, S. W. Bao, J. S. Zhang, and Y. Xu, “3D silicon neural probe with integrated optical fibers for optogenetic modulation,” *Lab on a Chip,* vol. 15, no. 14, pp. 2939-2949, 2015.

[23] H. B. Zhao, “Recent Progress of Development of Optogenetic Implantable Neural Probes,” *International Journal of Molecular Sciences,* vol. 18, no. 8, Aug, 2017.

[24] H. J. Lee, N. Choi, E. S. Yoon, and I. J. Cho, “MEMS devices for drug delivery,” *Advanced Drug Delivery Reviews,* vol. 128, pp. 132-147, Mar 15, 2018.

[25] G. Lehew, and M. A. L. Nicolelis, "State-of-the-Art Microwire Array Design for Chronic Neural Recordings in Behaving Animals," *Methods for Neural Ensemble Recordings*, Frontiers in Neuroscience nd and M. A. L. Nicolelis, eds., Boca Raton (FL), 2008.

[26] T.-D. TECHNOLOGIES. https://www.tdt.com/omnetics-based-electrodes.html.

[27] Plexon. "Thumbtack Probe," https://plexon.com/products/thumbtack-probe/.

[28] M. W. Merlo, R. L. Snyder, J. C. Middlebrooks, and M. Bachman, “Microelectrode arrays fabricated using a novel hybrid microfabrication method,” *Biomedical Microdevices,* vol. 14, no. 1, pp. 193-205, Feb, 2012.

[29] J. A. Kaltenbach, and G. L. Gerstein, “A rapid method for production of sharp tips on preinsulated microwires,” *Journal of Neuroscience Methods,* vol. 16, no. 4, pp. 283-288, 1986/06/01/, 1986.

[30] K. D. Wise, D. J. Anderson, J. F. Hetke, D. R. Kipke, and K. Najafi, “Wireless implantable microsystems: High-density electronic interfaces to the nervous system,” *Proceedings of the Ieee,* vol. 92, no. 1, pp. 76-97, Jan, 2004.

[31] K. D. Wise, J. B. Angell, and A. Starr, “An integrated-circuit approach to extracellular microelectrodes,” *IEEE Trans Biomed Eng,* vol. 17, no. 3, pp. 238-47, Jul, 1970.

[32] K. D. Wise, A. M. Sodagar, Y. Yao, M. N. Gulari, G. E. Perlin, and K. Najafi, “Microelectrodes, microelectronics, and implantable neural microsystems,” *Proceedings of the Ieee,* vol. 96, no. 7, pp. 1184-1202, Jul, 2008.

[33] K. Najafi, K. D. Wise, and T. Mochizuki, “A High-Yield Ic-Compatible Multichannel Recording Array,” *Ieee Transactions on Electron Devices,* vol. 32, no. 7, pp. 1206-1211, 1985.

[34] P. Norlin, M. Kindlundh, A. Mouroux, K. Yoshida, and U. G. Hofmann, “A 32-site neural recording probe fabricated by DRIE of SOI substrates,” *Journal of Micromechanics and Microengineering,* vol. 12, no. 4, pp. 414-419, Jul, 2002.

[35] K. C. Cheung, K. Djupsund, Y. Dan, and L. P. Lee, “Implantable multichannel electrode array based on SOI technology,” *Journal of Microelectromechanical Systems,* vol. 12, no. 2, pp. 179-184, Apr, 2003.

[36] NeuroNexus. "Standard Probes," http://neuronexus.com/products/neural-probes/standard-probes/?gclid=Cj0KCQjw5NnbBRDaARIsAJP-YR_dvtU4AUT-gpaXYKVN-fMxB7J7AGQvz1wOjq1sF3i4RPtK50Rv0rkaAgPMEALw_wcB.

[37] B. C. Raducanu, R. F. Yazicioglu, C. M. Lopez, M. Ballini, J. Putzeys, S. W. Wang, A. Andrei, V. Rochus, M. Welkenhuysen, N. van Helleputte, S. Musa, R. Puers, F. Kloosterman, C. Van Hoof, R. Fiath, I. Ulbert, and S. Mitra, “Time Multiplexed Active Neural Probe with 1356 Parallel Recording Sites,” *Sensors,* vol. 17, no. 10, Oct, 2017.

[38] J. K. Nguyen, D. J. Park, J. L. Skousen, A. E. Hess-Dunning, D. J. Tyler, S. J. Rowan, C. Weder, and J. R. Capadona, “Mechanically-compliant intracortical

implants reduce the neuroinflammatory response," *J Neural Eng,* vol. 11, no. 5, pp. 056014, Oct, 2014.

[39] J. K. Nguyen, D. J. Park, J. L. Skousen, A. E. Hess-Dunning, D. J. Tyler, S. J. Rowan, C. Weder, and J. R. Capadona, "Mechanically-compliant intracortical implants reduce the neuroinflammatory response," *Journal of Neural Engineering,* vol. 11, no. 5, Oct, 2014.

[40] L. J. Tang, M. H. Wang, H. C. Tian, X. Y. Kang, W. Hong, and J. Q. Liu, "Progress in Research of Flexible MEMS Microelectrodes for Neural Interface," *Micromachines,* vol. 8, no. 9, Sep, 2017.

[41] Y. Kato, M. Nishino, I. Saito, T. Suzuki, and K. Mabuchi, "Flexible intracortical neural probe with biodegradable polymer for delivering bioactive components," *2006 International Conference on Microtechnologies in Medicine and Biology*, pp. 143-+, 2006.

[42] F. Barz, P. Ruther, S. Takeuchi, and O. Paul, "Flexible Silicon-Polymer Neural Probe Rigidified by Dissolvable Insertion Vehicle for High-Resolution Neural Recording with Improved Duration," *2015 28th Ieee International Conference on Micro Electro Mechanical Systems (Mems 2015)*, pp. 636-639, 2015.

[43] S. Takeuchi, D. Ziegler, Y. Yoshida, K. Mabuchi, and T. Suzuki, "Parylene flexible neural probes integrated with microfluidic channels," *Lab on a Chip,* vol. 5, no. 5, pp. 519-523, 2005.

[44] M. C. Lo, S. W. Wang, S. Singh, V. B. Damodaran, H. M. Kaplan, J. Kohn, D. I. Shreiber, and J. D. Zahn, "Coating flexible probes with an ultra fast degrading

polymer to aid in tissue insertion," *Biomedical Microdevices,* vol. 17, no. 2, Apr, 2015.

[45] Z. L. Xiang, S. C. Yen, N. Xue, T. Sun, W. M. Tsang, S. S. Zhang, L. D. Liao, N. V. Thakor, and C. Lee, "Ultra-thin flexible polyimide neural probe embedded in a dissolvable maltose-coated microneedle," *Journal of Micromechanics and Microengineering,* vol. 24, no. 6, Jun, 2014.

[46] C. Hassler, N. Ehler, V. Singh, Y. J. Xie, N. Martini, R. D. Kirch, O. Prucker, J. Ruhe, U. G. Hofmann, and T. Stieglitz, "Fabrication and Implantation of Hydrogel Coated, Flexible Polyimide Electrodes," *2015 7th International Ieee/Embs Conference on Neural Engineering (Ner)*, pp. 561-564, 2015.

[47] C. Hassler, J. Guy, M. Nietzschmann, J. F. Staiger, and T. Stieglitz, "Chronic Intracortical Implantation of Saccharose-coated Flexible Shaft Electrodes into the Cortex of Rats," *2011 Annual International Conference of the Ieee Engineering in Medicine and Biology Society (Embc)*, pp. 644-647, 2011.

[48] M. Jeon, J. Cho, Y. K. Kim, D. Jung, E. S. Yoon, S. Shin, and I. J. Cho, "Partially flexible MEMS neural probe composed of polyimide and sucrose gel for reducing brain damage during and after implantation," *Journal of Micromechanics and Microengineering,* vol. 24, no. 2, Feb, 2014.

[49] D. P. O'Brien, T. R. Nichols, and M. G. Allen, "Flexible microelectrode arrays with integrated insertion devices," *14th Ieee International Conference on Micro Electro Mechanical Systems, Technical Digest*, pp. 216-219, 2001.

[50] T. D. Y. Kozai, and D. R. Kipke, "Insertion shuttle with carboxyl terminated self-assembled monolayer coatings for implanting flexible polymer neural probes in

the brain," *Journal of Neuroscience Methods,* vol. 184, no. 2, pp. 199-205, Nov 15, 2009.

[51] B. J. Kim, J. T. W. Kuo, S. A. Hara, C. D. Lee, L. Yu, C. A. Gutierrez, T. Q. Hoang, V. Pikov, and E. Meng, "3D Parylene sheath neural probe for chronic recordings," *Journal of Neural Engineering,* vol. 10, no. 4, Aug, 2013.

[52] S. A. Hara, B. J. Kim, J. T. W. Kuo, C. D. Lee, E. Meng, and V. Pikov, "Long-term stability of intracortical recordings using perforated and arrayed Parylene sheath electrodes," *Journal of Neural Engineering,* vol. 13, no. 6, Dec, 2016.

[53] A. Mercanzini, K. Cheung, D. L. Buhl, M. Boers, A. Maillard, P. Colin, J. C. Bensadoun, A. Bertsch, and P. Renaud, "Demonstration of cortical recording using novel flexible polymer neural probes," *Sensors and Actuators a-Physical,* vol. 143, no. 1, pp. 90-96, May 2, 2008.

[54] E. G. R. Kim, J. K. John, H. G. Tu, Q. L. Zheng, J. Loeb, J. S. Zhang, and Y. Xu, "A hybrid silicon-parylene neural probe with locally flexible regions," *Sensors and Actuators B-Chemical,* vol. 195, pp. 416-422, May, 2014.

[55] C. Xie, J. Liu, T. M. Fu, X. C. Dai, W. Zhou, and C. M. Lieber, "Three-dimensional macroporous nanoelectronic networks as minimally invasive brain probes," *Nature Materials,* vol. 14, no. 12, pp. 1286-1292, Dec, 2015.

[56] F. Wu, M. Im, and E. Yoon, "A flexible fish-bone-shaped neural probe strengthened by biodegradable silk coating for enhanced biocompatibility." pp. 966-969.

[57] T. Kim, A. Branner, T. Gulati, and S. F. Giszter, “Braided multi-electrode probes: mechanical compliance characteristics and recordings from spinal cords,” *Journal of Neural Engineering,* vol. 10, no. 4, Aug, 2013.

[58] T. N. Do, and Y. Visell, “Stretchable, Twisted Conductive Microtubules for Wearable Computing, Robotics, Electronics, and Healthcare,” *Scientific Reports,* vol. 7, May 11, 2017.

[59] Y. LeChasseur, S. Dufour, G. Lavertu, C. Bories, M. Deschenes, R. Vallee, and Y. De Koninck, “A microprobe for parallel optical and electrical recordings from single neurons in vivo,” *Nat Methods,* vol. 8, no. 4, pp. 319-25, Apr, 2011.

[60] F. Wu, E. Stark, P. C. Ku, K. D. Wise, G. Buzsaki, and E. Yoon, “Monolithically Integrated mu LEDs on Silicon Neural Probes for High-Resolution Optogenetic Studies in Behaving Animals,” *Neuron,* vol. 88, no. 6, pp. 1136-1148, Dec, 2015.

[61] T. I. Kim, J. G. McCall, Y. H. Jung, X. Huang, E. R. Siuda, Y. H. Li, J. Z. Song, Y. M. Song, H. A. Pao, R. H. Kim, C. F. Lu, S. D. Lee, I. S. Song, G. Shin, R. Al-Hasani, S. Kim, M. P. Tan, Y. G. Huang, F. G. Omenetto, J. A. Rogers, and M. R. Bruchas, “Injectable, Cellular-Scale Optoelectronics with Applications for Wireless Optogenetics,” *Science,* vol. 340, no. 6129, pp. 211-216, Apr 12, 2013.

[62] H. J. Lee, Y. Son, J. Kim, C. J. Lee, E. S. Yoon, and I. J. Cho, “A multichannel neural probe with embedded microfluidic channels for simultaneous in vivo neural recording and drug delivery,” *Lab on a Chip,* vol. 15, no. 6, pp. 1590-1597, 2015.

[63] G. Petit-Pierre, A. Bertsch, and P. Renaud, “Neural probe combining microelectrodes and a droplet-based microdialysis collection system for high temporal resolution sampling,” *Lab on a Chip,* vol. 16, no. 5, pp. 917-924, 2016.

[64] B. Liu, E. Kim, A. Meggo, S. Gandhi, H. Luo, S. Kallakuri, Y. Xu, and J. S. Zhang, “Enhanced biocompatibility of neural probes by integrating microstructures and delivering anti-inflammatory agents via microfluidic channels,” *Journal of Neural Engineering,* vol. 14, no. 2, Apr, 2017.

[65] M. J. Madou, *Fundamentals of microfabrication : the science of miniaturization*, 2nd ed., Boca Raton: CRC Press, 2002.

[66] E. Kim, H. Tu, C. Lv, H. Jiang, H. Yu, and Y. Xu, “A robust polymer microcable structure for flexible devices,” *Applied Physics Letters,* vol. 102, no. 3, pp. 033506-033506-4, 2013.

[67] M. W. Shinwari, D. Zhitomirsky, I. A. Deen, P. R. Selvaganapathy, M. J. Deen, and D. Landheer, “Microfabricated Reference Electrodes and their Biosensing Applications,” *Sensors,* vol. 10, no. 3, pp. 1679-1715, Mar, 2010.

[68] B. J. Polk, A. Stelzenmuller, G. Mijares, W. MacCrehan, and M. Gaitan, “Ag/AgCl microelectrodes with improved stability for microfluidics,” *Sensors and Actuators B-Chemical,* vol. 114, no. 1, pp. 239-247, Mar 30, 2006.

[69] I. Y. Huang, and R. S. Huang, “Fabrication and characterization of a new planar solid-state reference electrode for ISFET sensors,” *Thin Solid Films,* vol. 406, no. 1-2, pp. 255-261, Mar 1, 2002.

[70] W. Y. Liao, and T. C. Chou, “Fabrication of a planar-form screen-printed solid electrolyte modified Ag/AgCl reference electrode for application in a

potentiometric biosensor," *Analytical Chemistry,* vol. 78, no. 12, pp. 4219-4223, Jun 15, 2006.

[71] H. Suzuki, T. Hirakawa, S. Sasaki, and I. Karube, "Micromachined liquid-junction Ag/AgCl reference electrode," *Sensors and Actuators B: Chemical,* vol. 46, no. 2, pp. 146-154, 2/15/, 1998.

[72] H. Suzuki, H. Shiroishi, S. Sasaki, and I. Karube, "Microfabricated Liquid Junction Ag/AgCl Reference Electrode and Its Application to a One-Chip Potentiometric Sensor," *Analytical Chemistry,* vol. 71, no. 22, pp. 5069-5075, 1999/11/01, 1999.

[73] H. G. Tu, X. Y. Chen, X. C. Feng, and Y. Xu, "A post-CMOS compatible smart yarn technology based on SOI wafers," *Sensors and Actuators a-Physical,* vol. 233, pp. 397-404, Sep, 2015.

[74] E. Kim, H. Tu, C. Lv, H. Q. Jiang, H. Y. Yu, and Y. Xu, "A robust polymer microcable structure for flexible devices," *Applied Physics Letters,* vol. 102, no. 3, Jan, 2013.

[75] H. Gerischer, "Reference Electrodes: Theory and Practice, herausgeg. von D. J. G. Ives und G. J. Janz. Academic Press, New York—London 1961. 1. Aufl., XI, 651 S., zahlr. Abb. und Tab., geb. £ 7.3.—," *Angewandte Chemie,* vol. 75, no. 18, pp. 879-879, 21/1963, 1961.

[76] T. Kitade, K. Kitamura, S. Takegami, Y. Miyata, M. Nagatomo, T. Sakaguchi, and M. Furukawa, "Needle-type ultra micro silver/silver chloride reference electrode for use in micro-electrochemistry," *Anal Sci,* vol. 21, no. 8, pp. 907-12, Aug, 2005.

[77] E. Kim, “DEVELOPMENT OF ADVANCED MULTIFUNCTIONAL NEURAL INTERFACE DEVICES,” Dissertation, BIOMEDICAL ENGINEERING, Wayne State University, Detroit, Michigan, 2016.

[78] S. Yao, M. Wang, and M. Madou, “A pH electrode based on melt-oxidized iridium oxide,” *Journal of the Electrochemical Society,* vol. 148, no. 4, pp. H29-H36, Apr, 2001.

[79] W. D. Huang, H. Cao, S. Deb, M. Chiao, and J. C. Chiao, “A flexible pH sensor based on the iridium oxide sensing film,” *Sensors and Actuators a-Physical,* vol. 169, no. 1, pp. 1-11, Sep, 2011.

[80] W. Olthuis, M. A. M. Robben, P. Bergveld, M. Bos, and W. E. Vanderlinden, “PH SENSOR PROPERTIES OF ELECTROCHEMICALLY GROWN IRIDIUM OXIDE,” *Sensors and Actuators B-Chemical,* vol. 2, no. 4, pp. 247-256, Oct, 1990.

[81] R. K. Jaworski, J. A. Cox, and B. R. Strohmeier, “Characterization of oxide films electrochemically deposited from solutions of palladium chloride and sodium hexachloroiridate,” *Journal of Electroanalytical Chemistry,* vol. 325, no. 1–2, pp. 111-123, 3/23/, 1992.

[82] Z. Fekete, “Recent advances in silicon-based neural microelectrodes and microsystems: a review,” *Sensors and Actuators B: Chemical,* vol. 215, no. Supplement C, pp. 300-315, 2015/08/01/, 2015.

[83] K. C. Cheung, “Implantable microscale neural interfaces,” *Biomedical Microdevices,* vol. 9, no. 6, pp. 923-938, December 01, 2007.

[84] J. K. Chapin, “Using multi-neuron population recordings for neural prosthetics,” *Nature Neuroscience,* vol. 7, no. 5, pp. 452-455, May, 2004.

[85] A. Branner, R. B. Stein, E. Fernandez, Y. Aoyagi, and R. A. Normann, “Long-term stimulation and recording with a penetrating microelectrode array in cat sciatic nerve,” *Ieee Transactions on Biomedical Engineering,* vol. 51, no. 1, pp. 146-157, Jan, 2004.

[86] Z. Fekete, and A. Pongrácz, “Multifunctional soft implants to monitor and control neural activity in the central and peripheral nervous system: A review,” *Sensors and Actuators B: Chemical,* vol. 243, no. Supplement C, pp. 1214-1223, 2017/05/01/, 2017.

[87] A. Altuna, L. Menendez de la Prida, E. Bellistri, G. Gabriel, A. Guimerá, J. Berganzo, R. Villa, and L. J. Fernández, “SU-8 based microprobes with integrated planar electrodes for enhanced neural depth recording,” *Biosensors and Bioelectronics,* vol. 37, no. 1, pp. 1-5, 2012/08/01/, 2012.

[88] D. C. Rodger, A. J. Fong, W. Li, H. Ameri, A. K. Ahuja, C. Gutierrez, I. Lavrov, H. Zhong, P. R. Menon, E. Meng, J. W. Burdick, R. R. Roy, V. R. Edgerton, J. D. Weiland, M. S. Humayun, and Y.-C. Tai, “Flexible parylene-based multielectrode array technology for high-density neural stimulation and recording,” *Sensors and Actuators B: Chemical,* vol. 132, no. 2, pp. 449-460, 2008/06/16/, 2008.

[89] V. Castagnola, E. Descamps, A. Lecestre, L. Dahan, J. Remaud, L. G. Nowak, and C. Bergaud, “Parylene-based flexible neural probes with PEDOT coated surface for brain stimulation and recording,” *Biosensors and Bioelectronics,* vol. 67, no. Supplement C, pp. 450-457, 2015/05/15/, 2015.

[90] T. Stieglitz, H. Beutel, M. Schuettler, and J. U. Meyer, “Micromachined, Polyimide-Based Devices for Flexible Neural Interfaces,” *Biomedical Microdevices,* vol. 2, no. 4, pp. 283-294, Dec, 2000.

[91] M. Hajj-Hassan, V. P. Chodavarapu, and S. Musallam, “Microfabrication of ultra-long reinforced silicon neural electrodes,” *Micro & Nano Letters,* vol. 4, no. 1, pp. 53-58, Mar, 2009.

[92] Z. Fekete, Z. Hajnal, G. Márton, P. Fürjes, and A. Pongrácz, “Fracture analysis of silicon microprobes designed for deep-brain stimulation,” *Microelectronic Engineering,* vol. 103, no. Supplement C, pp. 160-166, 2013/03/01/, 2013.

[93] Zolt, #225, and n. Fekete, “Technology of ultralong deep brain fluidic microelectrodes combined with etching-before-grinding,” *Microsyst. Technol.,* vol. 21, no. 2, pp. 341-344, 2015.

[94] A. Pongrácz, Z. Fekete, G. Márton, Z. Bérces, I. Ulbert, and P. Fürjes, “Deep-brain silicon multielectrodes for simultaneous in vivo neural recording and drug delivery,” *Sensors and Actuators B: Chemical,* vol. 189, no. Supplement C, pp. 97-105, 2013/12/01/, 2013.

[95] Z. Fekete, E. Pálfi, G. Márton, M. Handbauer, Z. Bérces, I. Ulbert, A. Pongrácz, and L. Négyessy, “Combined in vivo recording of neural signals and iontophoretic injection of pathway tracers using a hollow silicon microelectrode,” *Sensors and Actuators B: Chemical,* vol. 236, no. Supplement C, pp. 815-824, 2016/11/29/, 2016.

[96] NeuroNexus. http://neuronexus.com/products/primate-large-brain/vector-array/.

[97] Plexon. https://plexon.com/products/plexon-electrodes-probes-and-arrays/.

[98] F. Pothof, L. Bonini, M. Lanzilotto, A. Livi, L. Fogassi, G. A. Orban, O. Paul, and P. Ruther, “Chronic neural probe for simultaneous recording of single-unit, multi-unit, and local field potential activity from multiple brain sites,” *Journal of Neural Engineering,* vol. 13, no. 4, pp. 046006, 2016.

[99] L. W. Tien, F. Wu, M. D. Tang-Schomer, E. Yoon, F. G. Omenetto, and D. L. Kaplan, “Silk as a Multifunctional Biomaterial Substrate for Reduced Glial Scarring around Brain-Penetrating Electrodes,” *Advanced Functional Materials,* vol. 23, no. 25, pp. 3185-3193, Jul 5, 2013.

[100] A. Lecomte, V. Castagnola, E. Descamps, L. Dahan, M. C. Blatché, T. M. Dinis, E. Leclerc, C. Egles, and C. Bergaud, “Silk and PEG as means to stiffen a parylene probe for insertion in the brain: toward a double time-scale tool for local drug delivery,” *Journal of Micromechanics and Microengineering,* vol. 25, no. 12, pp. 125003, 2015.

[101] K. K. Lee, J. P. He, A. Singh, S. Massia, G. Ehteshami, B. Kim, and G. Raupp, “Polyimide-based intracortical neural implant with improved structural stiffness,” *Journal of Micromechanics and Microengineering,* vol. 14, no. 1, pp. 32-37, Jan, 2004.

[102] E. M. Maynard, E. Fernandez, and R. A. Normann, “A technique to prevent dural adhesions to chronically implanted microelectrode arrays,” *Journal of Neuroscience Methods,* vol. 97, no. 2, pp. 93-101, Apr 15, 2000.

[103] J. F. Hetke, J. L. Lund, K. Najafi, K. D. Wise, and D. J. Anderson, “Silicon Ribbon Cables for Chronically Implantable Microelectrode Arrays,” *Ieee Transactions on Biomedical Engineering,* vol. 41, no. 4, pp. 314-321, Apr, 1994.

[104] A. Gilletti, and J. Muthuswamy, “Brain micromotion around implants in the rodent somatosensory cortex,” *Journal of Neural Engineering,* vol. 3, no. 3, pp. 189-195, Sep, 2006.

[105] R. Biran, D. C. Martin, and P. A. Tresco, “The brain tissue response to implanted silicon microelectrode arrays is increased when the device is tethered to the skull,” *Journal of Biomedical Materials Research Part A,* vol. 82a, no. 1, pp. 169-178, Jul, 2007.

[106] A. Ersen, S. Elkabes, D. S. Freedman, and M. Sahin, “Chronic tissue response to untethered microelectrode implants in the rat brain and spinal cord,” *Journal of Neural Engineering,* vol. 12, no. 1, Feb, 2015.

[107] V. Sankar, J. C. Sanchez, E. McCumiskey, N. Brown, C. R. Taylor, G. J. Ehlert, H. A. Sodano, and T. Nishida, “A highly compliant serpentine shaped polymide interconnect for front-end strain relief in chronic neural implants,” *Frontiers in Neurology,* vol. 4, 2013.

[108] H. E. Tu, and Y. Xu, “A post silicon-on-insulator compatible smart tube technology,” *Lab on a Chip,* vol. 13, no. 6, pp. 1027-1030, 2013.

[109] Z. Zhao, H. Tu, E. G. R. Kim, B. F. Sloane, and Y. Xu, “A flexible Ag/AgCl micro reference electrode based on a parylene tube structure,” *Sensors and Actuators B: Chemical,* vol. 247, pp. 92-97, 8//, 2017.

[110] Z. Fekete, A. Pongrácz, P. Fürjes, and G. Battistig, “Improved process flow for buried channel fabrication in silicon,” *Microsystem Technologies,* vol. 18, no. 3, pp. 353-358, 2012.

[111] W. H. Lee, T. R. Slaney, R. W. Hower, and R. T. Kennedy, “Microfabricated Sampling Probes for in Vivo Monitoring of Neurotransmitters,” *Analytical Chemistry,* vol. 85, no. 8, pp. 3828-3831, 2013/04/16, 2013.

[112] J. S. Zhang, and X. G. Zhang, “Electrical stimulation of the dorsal cochlear nucleus induces hearing in rats,” *Brain Research,* vol. 1311, pp. 37-50, Jan, 2010.

[113] Z. Fekete, A. Németh, G. Márton, I. Ulbert, and A. Pongrácz, “Experimental study on the mechanical interaction between silicon neural microprobes and rat dura mater during insertion,” *Journal of Materials Science: Materials in Medicine,* vol. 26, no. 2, pp. 70, January 29, 2015.

[114] S. B. Goncalves, A. C. Peixoto, A. F. Silva, and J. H. Correia, “Fabrication and mechanical characterization of long and different penetrating length neural microelectrode arrays,” *Journal of Micromechanics and Microengineering,* vol. 25, no. 5, May, 2015.

[115] W. Jensen, K. Yoshida, and U. G. Hofmann, “In-vivo implant mechanics of flexible, silicon-based ACREO microelectrode arrays in rat cerebral cortex,” *Ieee Transactions on Biomedical Engineering,* vol. 53, no. 5, pp. 934-940, May, 2006.

[116] *Parylene Data Sheet*, Specialty Coating System, Indianapolis, Indiana, Parylene Data Sheet, Specialty Coating System, Indianapolis, Indiana, 2007.

[117] J. R. Davis, *Stainless Steels*: ASM International, 1994.

[118] A. A. Sharp, A. M. Ortega, D. Restrepo, D. Curran-Everett, and K. Gall, “In Vivo Penetration Mechanics and Mechanical Properties of Mouse Brain Tissue at

Micrometer Scales," *Ieee Transactions on Biomedical Engineering,* vol. 56, no. 1, pp. 45-53, Jan, 2009.

[119] K. N. Jessica, J. P. Daniel, L. S. John, E. H.-D. Allison, J. T. Dustin, J. R. Stuart, W. Christoph, and R. C. Jeffrey, "Mechanically-compliant intracortical implants reduce the neuroinflammatory response," *Journal of Neural Engineering,* vol. 11, no. 5, pp. 056014, 2014.

[120] J. K. John, E. Kim, H. Tu, J. Zhang, J. A. Loeb, and Y. Xu, "Multifunctional chronic 3D electrode arrays based on a simple folding process." pp. 1476-1479.

[121] J. John, Y. F. Li, J. S. Zhang, J. A. Loeb, and Y. Xu, "Microfabrication of 3D neural probes with combined electrical and chemical interfaces," *Journal of Micromechanics and Microengineering,* vol. 21, no. 10, Oct, 2011.

[122] B. S. Shim, W. Chen, C. Doty, C. L. Xu, and N. A. Kotov, "Smart Electronic Yarns and Wearable Fabrics for Human Biomonitoring made by Carbon Nanotube Coating with Polyelectrolytes," *Nano Letters,* vol. 8, no. 12, pp. 4151-4157, Dec, 2008.

[123] P. Mostafalu, M. Akbari, K. A. Alberti, Q. B. Xu, A. Khademhosseini, and S. R. Sonkusale, "A toolkit of thread-based microfluidics, sensors, and electronics for 3D tissue embedding for medical diagnostics," *Microsystems & Nanoengineering,* vol. 2, Jul 18, 2016.

[124] Z. H. Tang, S. H. Jia, F. Wang, C. S. Bian, Y. Y. Chen, Y. L. Wang, and B. Li, "Highly Stretchable Core-Sheath Fibers via Wet-Spinning for Wearable Strain Sensors," *Acs Applied Materials & Interfaces,* vol. 10, no. 7, pp. 6624-6635, Feb 21, 2018.

[125] Z. T. Li, and Z. L. Wang, “Air/Liquid-Pressure and Heartbeat-Driven Flexible Fiber Nanogenerators as a Micro/Nano-Power Source or Diagnostic Sensor,” *Advanced Materials,* vol. 23, no. 1, pp. 84-89, Jan 4, 2011.

[126] M. Zhang, K. R. Atkinson, and R. H. Baughman, “Multifunctional carbon nanotube yarns by downsizing an ancient technology,” *Science,* vol. 306, no. 5700, pp. 1358-1361, Nov 19, 2004.

[127] A. B. Dalton, S. Collins, E. Munoz, J. M. Razal, V. H. Ebron, J. P. Ferraris, J. N. Coleman, B. G. Kim, and R. H. Baughman, “Super-tough carbon-nanotube fibres - These extraordinary composite fibres can be woven into electronic textiles.,” *Nature,* vol. 423, no. 6941, pp. 703-703, Jun 12, 2003.

[128] M. D. Lima, N. Li, M. J. de Andrade, S. L. Fang, J. Oh, G. M. Spinks, M. E. Kozlov, C. S. Haines, D. Suh, J. Foroughi, S. J. Kim, Y. S. Chen, T. Ware, M. K. Shin, L. D. Machado, A. F. Fonseca, J. D. W. Madden, W. E. Voit, D. S. Galvao, and R. H. Baughman, “Electrically, Chemically, and Photonically Powered Torsional and Tensile Actuation of Hybrid Carbon Nanotube Yarn Muscles,” *Science,* vol. 338, no. 6109, pp. 928-932, Nov 16, 2012.

[129] Z. G. Zhao, E. Kim, H. Luo, J. S. Zhang, and Y. Xu, “Flexible deep brain neural probes based on a parylene tube structure,” *Journal of Micromechanics and Microengineering,* vol. 28, no. 1, Jan, 2018.

[130] R. L. Parker, and A. Krinsky, “Electrical Resistance-Strain Characteristics of Thin Evaporated Metal Films,” *Journal of Applied Physics,* vol. 34, no. 9, pp. 2700-&, 1963.

[131] B. Hok, R. Nyholm, O. Groth, and P. A. Tove, “Study of Discontinuous Au Films with Respect to Strain Gauge Applications,” *Thin Solid Films,* vol. 17, no. 1, pp. 113-121, 1973.

ABSTRACT

PARYLENE BASED FLEXIBLE MULTIFUNCTIONAL BIOMEDICAL PROBES AND THEIR APPLICATIONS

by

ZHIGUO ZHAO

August 2020

Advisor: Dr. Yong Xu

Major: Electrical and Computer Engineering

Degree: Doctor of Philosophy

MEMS (Micro Electro Mechanical System) based flexible devices have been studied for decades, and they are rapidly being incorporated into modern society in various forms such as flexible electronics and wearable devices. Especially in neuroscience, flexible interfaces provide tremendous possibilities and opportunities to produce reliable, scalable and biocompatible instruments for better exploring neurotransmission and neurological disorders. Of all the types of biomedical instruments such as electroencephalography (EEG) and electrocorticography (ECoG), MEMS-based needle-shape probes have been actively studied in recent years due to their better spatial resolution, selectivity, and sensitivity in chronical invasive physiology monitoring. In order to address the inherent issue of invasiveness that causes tissue damage, research has been made on biocompatible materials, implanting methods and probe structural design.

In this dissertation, different types of microfabricated probes for various applications are reviewed. General methods for some key fabrication steps include photolithography patterning, chemical vapor deposition, metal deposition and dry etching are covered in detail. Likewise, three major achievements, which aim to the tagets of

flexibility, functionality and mechanical property are introduced and described in detail from chapter 3 to 5. The essential fabrication processes based on XeF_2 isotropic silicon etching and parylene conformal deposition are covered in detail, and a set of characterization is summarized.

AUTOBIOGRAPHICAL STATEMENT

Zhiguo Zhao got his bachelor's degree in mechanical engineering from Southwest Jiaotong University in Chengdu, China in 2008. During his work on his bachelor's degree, he worked on the project on design and fabrication of mechanical mold for various products such as cell phones. He got his Master of Science degree in electrical and computer engineering from Kyungpook National University in South Korea in 2010. During his work on his master's degree, he worked on the project of design and development of an amorphous Si-based thermal infrared detector based on MEMS technology. He joined Photronics.Inc, an advanced semiconductor manufacturer, and worked as a photomask process engineer from 2010 to 2014.

Zhiguo Zhao started his Ph.D. program in 2015. His research during his Ph.D. work at Wayne State has focused on biomedical microprobes design, fabrication, and implementation. During his time with the Wayne State University College of Engineering, he worked with state-of-the-art instrumentation for microfabrication at the LNF cleanroom facility at the University of Michigan.

Zhiguo's intended future career is microsystem research and development based on MEMS technology.